Marche Polytechnic University

Master of Science Course in Environmental Engineering

Lagrangian Measurements Of Wave-Induced Currents: Relation Between Infragravity Waves And Drift Velocities

Advisor:

Prof. Postacchini Matteo

Student:

Marconi Alessandro

Co-Advisors:

Dott. Melito Lorenzo

Prof. Kalisch Henrik

A.Y. 2023 / 2024

Contents

List of figures

List of symbols

w: vertical component of the velocity vector

u: horizontal component of the velocity vector

T: Wave period

h: Wave height

a: Wave amplitude

ω: angular frequency of the wave

k: Wave number

g: Gravity acceleration

τ: Response time

$\emptyset$: Velocity potential

U_L: Drif velocities

D_x: Horizontal Drift

T_L: Lagrangian period

UU: Reverse current

Abstract

The thesis investigates the dynamics generated by monochromatic and infragravity waves (IG). Over the past decade, there has been growing interest in IG waves, as demonstrated by the increase in literature on the topic [2].

Since the time of Stokes and his research on stationary progressive surface waves in 1847, there has been a focus on the trajectories of fluid particles and the associated mass flux. However, recent studies indicate that, especially in waves propagating over a shear flow, a net Eulerian flow can develop as opposed to Stokes drift [9]. Some studies suggest that in deep-water environments, net Eulerian flow may cancel the Lagrangian Stokes drift on a pointwise basis.

In recent field measurements, it has been observed that the drift velocity correlates positively with the local mean depth of the fluid i.e. a wave with a rise has a large forward drift, while a wave with a fall has a net negative drift [3].

The study in question aims to examine what has been observed in the field through laboratory experiments conducted in a wave channel. Monochromatic and bichromatic waves of different characteristics were performed in the hydraulic laboratory of the Polytechnic University of Marche, using a wave channel (size: 50m×1m×1.3m) with a piston wave generator, the use of a camera high resolution and light sheet created by a halogen lamp and ground chili peppers as the neutral seeding.

Two experiments were conducted: in the first test a monochromatic wave characterized by a height of 3 cm and a period of 1 s; in the second test, a bichromatic wave composed by the same monochromatic wave as in the first test, superimposed to a long wave (height of 0.3 cm and a period of 10s) has been used. Focus was given on the particle trajectories and the longitudinal distribution of the velocity along the vertical.

The bichromatic waves were generated by superimposing a shorter wave onto a longer wave, attempting to replicate the natural combination of shorter waves with longer infragravity waves typical of the coastal region.

Detailed analysis of trajectories and drift velocities provides an in-depth perspective on the behavior of such elements along the trough and peak of the

bichromatic wave.

Finally, the results obtained from this type of approach were then compared with previous research by Grue and Kolaas [6].

Riassunto

La tesi indaga le dinamiche generate dalle onde monocromatiche e di infragravità (IG). Negli ultimi dieci anni si è assistito ad un crescente interesse per le onde IG, come dimostrato dall'aumento della letteratura sull'argomento [2].

Sin dai tempi di Stokes e della sua ricerca sulle onde superficiali stazionarie progressive nel 1847, ci si è concentrati sulle traiettorie delle particelle fluide e sul flusso di massa associato. Tuttavia, studi recenti indicano che, soprattutto nelle onde che si propagano lungo un flusso di taglio, può svilupparsi un flusso euleriano netto in contrapposizione alla deriva di Stokes [9]. Alcuni studi suggeriscono che in ambienti di acque profonde, il flusso euleriano netto può annullare la deriva lagrangiana di Stokes su base puntiforme.

In recenti misurazioni sul campo, è stato osservato che la velocità di deriva è correlata positivamente con la profondità media locale del fluido, ovvero un'onda con un aumento ha una grande deriva in avanti, mentre un'onda con una caduta ha una deriva netta negativa [3].

Lo studio in questione si propone di esaminare quanto osservato sul campo attraverso esperimenti di laboratorio condotti in un canale d'onda. Onde monocromatiche e bicromatiche di diverse caratteristiche sono state eseguite nel laboratorio idraulico dell'Università Politecnica delle Marche, utilizzando un canale d'onda (dimensioni: 50m×1m×1,3m) con un generatore di onde a pistone, l'uso di una telecamera ad alta risoluzione e un foglio luminoso creato da una lampada alogena e peperoncini macinati come semina neutra.

Sono stati condotti due esperimenti: nella prima prova un'onda monocromatica caratterizzata da un'altezza di 3 cm e un periodo di 1 s; nella seconda prova è stata utilizzata un'onda bicromatica composta dalla stessa onda monocromatica della prima prova, sovrapposta ad un'onda lunga (altezza 0,3 cm e periodo 10s). L'attenzione è stata posta sulle traiettorie delle particelle e sulla distribuzione longitudinale della velocità lungo la verticale.

Le onde bicromatiche sono state generate sovrapponendo un'onda più corta a un'onda più lunga, cercando di replicare la combinazione naturale di onde più corte con onde di infragravità più lunghe tipica della regione costiera.

L'analisi dettagliata delle traiettorie e delle velocità di deriva fornisce una prospettiva approfondita sul comportamento di tali elementi lungo la valle e il picco dell'onda bicromatica.

Infine, i risultati ottenuti da questo tipo di approccio sono stati poi confrontati con le precedenti ricerche di Grue e Kolaas [6].

Motivation and thesis outline

This thesis aims to complement field observations regarding wave motion fields under monochromatic and bichromatic waves through laboratory experiments performed in a wave channel. The main objective is to investigate the dynamics generated by monochromatic and infragravity waves, each were tested with different characteristics. The research was conducted through a specific experimental campaign at the Hydraulics and Maritime Construction Laboratory of the Polytechnic University of Marche, located in Ancona. Through the methodical execution of experiments in the laboratory and the use of dedicated calculation software, the thesis aims to explore the behaviour of the particles inside the channel, focusing on these two different configurations. The selected water depth was h = 12 cm, over which several wave characteristics were tested (wave height $a1$ = 3 cm), period $T1$ = 1 s. The bichromatic wave was produced by superimposing a shorter wave onto a longer wave. The shorter component was based on the same characteristics of the above-mentioned monochromatic wave (*a1, T1*), while the longer component was characterized by a smaller wave height and a longer period (*a2 = 0.3 cm, T2 = 10s*), with the aim to reproduce the natural combination of shorter sea waves with longer infragravity waves that typically occur in the nearshore region [12]. The present thesis was inspired by research conducted by the University of Bergen, Norway, Department of Mathematics and the Institute of Coastal Ocean Dynamics, HelmholtzZentrum Hereon, Geesthacht, Germany [3]. The relative influence of wave-by-wave variations of mean water level, wave height and incipient wave breaking on the mass transport properties of waves in the surf zone was studied. It has been quantitatively demonstrated that a high local mean water level positively correlates with an increase in Lagrangian mass transport to the free surface. Eulerian measurements of Acoustic doppler velocimeter (ADV) in the fluid column suggest that wave-by-wave depth-integrated mass transport is also positively correlated with local mean water level and is only weakly related to wave height and wave breaking events. The main measurement system in this study [3] was a stereo imaging system, which was able

to resolve the movements of floating surface tracers (oranges) on the undulating water surface within the surf zone. Additional supporting wind and wave data were obtained from a combination of in situ and remote sensing measurement systems, including bottom-mounted pressure wave gauges, a bottom-mounted ADV, bottom-mounted optical pole wave gauges and drone imagery (Figure 1).

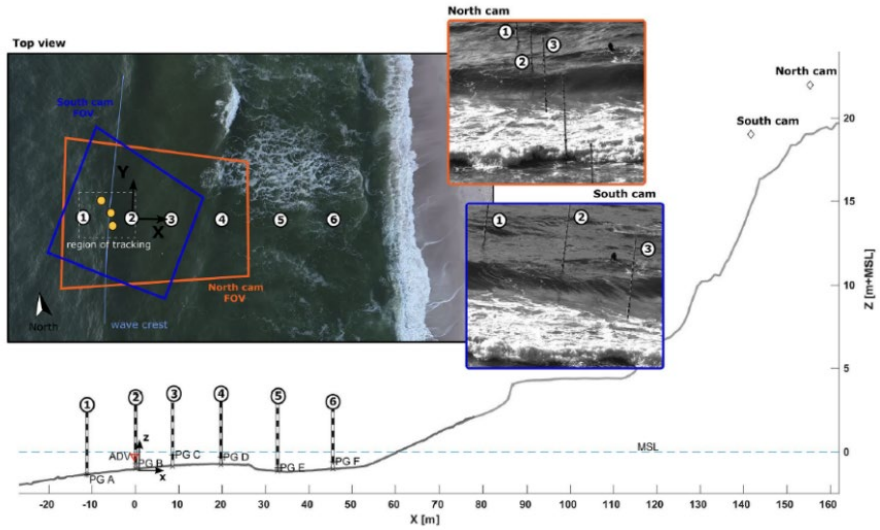

Figure 1: Lagrangian motion of a particle tracer in the same time window as the free-surface data in the left panel. The blue and yellow waves feature instantaneous wave set-up and corresponding strong shoreward Lagrangian transport while the red wave features set-down and backward drift. The black rectangle indicates the tracer position when tracking commenced, and the solid black square indicates the final tracer position. There are some gaps in the tracer positions in cases when the tracer was not visible in both cameras. Due to inherent differences between Eulerian and Lagrangian measurements as well as tracer drift, there are slight differences in the observed wave height between the upper left and upper right panels. (Bjørnestad et al.2021).

Lagrangian particle paths were recorded in individual waves in the surf zone as shown in Figure 2. To better understand the particle paths observed in situ, comparisons were made with a theoretical wave model.

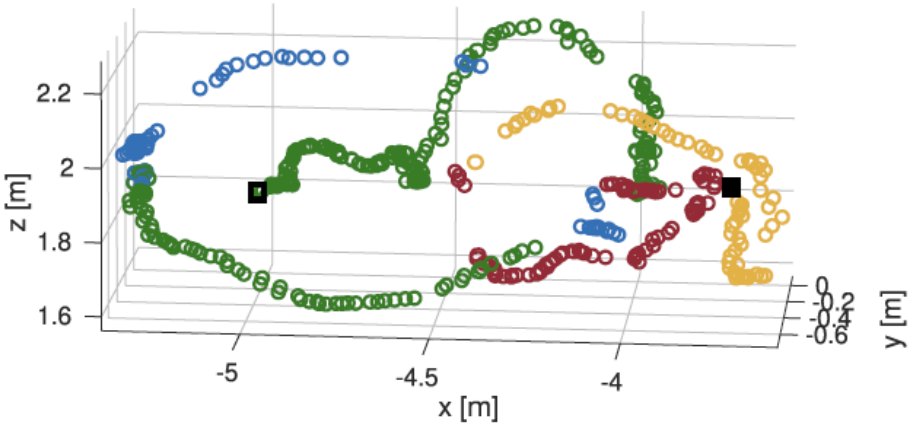

Figure 2: Lagrangian motion of a particle tracer in the same time window as the free-surface data in the left panel. The blue and yellow waves feature instantaneous wave set-up and corresponding strong shoreward Lagrangian transport while the red wave features set-down and backward drift. The black rectangle indicates the tracer position when tracking commenced, and the solid black square indicates the final tracer position. There are some gaps in the tracer positions in cases when the tracer was not visible in both cameras. Due to inherent differences between Eulerian and Lagrangian measurements as well as tracer drift, there are slight differences in the observed wave height between the upper left and upper right panels. (Bjørnestad et al.2021).

The close relationship between the Lagrangian velocities on the free surface and the oscillations observed in the mean water level here points to the possibility that the dissipation of infragravity waves may also arise from gravity waves. Observation of the mean water level suggests that dissipation of infragravity waves could occur through the breaking of gravity waves, with subsequent dispersion of the infragravity field caused by the broken shorter waves. Indeed, the Lagrangian velocity on the free surface can be interpreted as a facilitator of shorter wave breaking, in line with the kinematic criterion for wave breaking [10].

The thesis is divided into five distinct chapters.
The first, dedicated to State of the art, presents a brief summary of past research and a broad overview of the importance of the waves studied is also provided.

The second chapter, the experimental setup. This section provides a comprehensive exploration of the methodologies employed in the study.

In the third chapter, the results deriving from the experimental analysis are examined in depth.

In Chapter 4, Discussion, an in-depth comparison of the obtained results is provided, focusing mainly on the comparison between the bichromatic and monochromatic configurations.

In Chapter 5, Conclusions, some final considerations emerging from the study and comparison just conducted are presented.

1 State of the art

As a wave propagates, the fluid particles experience a net transport. This transport is called the Stokes drift and was first described around 170 years ago [1, 5]. The magnitude of the transport is largest at the surface and decays with depth [11].
Since the work of Stokes on steady progressive surface waves (Stokes, 1847), there has been interest in fluid particle trajectories and associated mass flux. The original result obtained by Stokes was based on linear theory, and implied that there is a net forward drift in the fluid beneath a propagating surface wave. In the non-dimensional case, the drift velocity for a sinusoidal wave on a fluid of depth h is given by

$$\bar{U}_L = a^2 \omega k \frac{\cosh\left(2k(z+h)\right)}{2sinh^2 kh} \quad where \sqrt{gk \tanh kh}$$

Recent works suggest that in many cases, particularly in waves propagating over a shear flow, a net Eulerian flow may develop, which opposes to the Stokes drift. Monismith et al. (2007) [9] have presented several sets of laboratory measurements where the averaged Lagrangian wave drift velocity has been found to be zero across water column.

Mean flows under surface gravity waves

Reference	Type of flow	Flow	kH
Nepf *et al.* (various)	Open (pumped)	Turbulent	1.4 to 4
Cowen *et al.* (various)	Open (pumped)	Turbulent	2.1
Klopman (1994)	Open (pumped)	Turbulent	1.04
Jiang & Street (1991)	Closed (zero transport)	Laminar	4
Swan (1990)	Closed (zero transport)	Laminar	1.8
Thais & Magnaudet (1996)	Closed (zero transport)	Laminar	4

Figure 3: Mean flows under surface gravity waves.(Monismith et al.2007).

This implies that an Eulerian mean velocity cancel locally the Stokes drift in those experiments. The results of Monismith et al. have primarily been found in the combined cases with waves propagating on constant and sheared currents, where in the experiments by Klopman, referred to in Groeneweg & Klopman (1998), and those of Nepf et al. (1995), the underlying channel flows were turbulent, where the effects of the bottom boundary layer could be felt throughout the depth at earlier distance and time compared to the case where waves propagate along a fluid layer

otherwise at rest.

However, not all experiments reported in the literature conform with the measurements obtaining a vanishing Lagrangian wave drift velocity. Groeneweg & Klopman (1998),for instance, observed that.

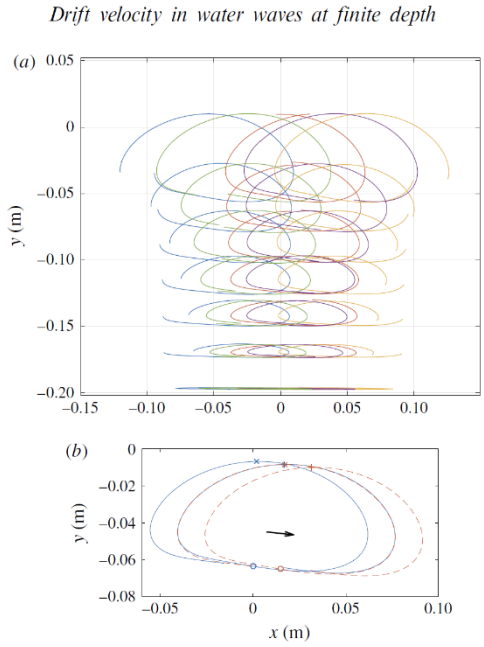

Figure 4: (a) Particle paths for several vertical positions and phases. (b) Particle path for one period backward and forward integration (blue solid line) and shifted by the drift during one period (red dashed line), where the black arrow indicates the drift distance (x0; y0). (J. Grue and J. Kolaas 2017).

The differences in the results point to conflicts between the various experimental observations, including differences in the nonlinear wave and mean flow interaction processes as well as the boundary conditions. Further, Grue & Kolaas (2017) [6] saw that comparisons to calculations by the inviscid strongly nonlinear Fenton method and the second-order theory show that the streaming velocities in the boundary layers below the wave surface and above the fluid bottom contribute to a strongly enhanced forward drift velocity and excess period. The experimental drift velocity shear becomes more than twice that obtained by the Fenton method, which again is approximately twice that of the second-order theory close to the surface. There is no mass flux of the periodic experimental waves and no pressure gradient. The particle paths are closed at the two vertical positions where $U_L = 0$. Moreover, Eulerian and Lagrangian measurements of orbital velocities in waves approaching a beach are analyzed with the goal of understanding the relative

influence of wave-by-wave variations in mean water level, wave height and incipient wave breaking on mass transport properties of waves in the surf zone. It is shown quantitatively that elevated local mean-water level correlates positively with increased Lagrangian mass transport at the free surface.

The present work aims to investigate what was observed in the field by Kalisch et al. [3] through laboratory experiments conducted in a wave flume, where monochromatic and biochromatic waves of different characteristics were run.

1.1 Infragravity Waves

Over the last decade, numerous studies have integrated numerical modeling with either field or laboratory experiments to enhance comprehension of the processes governing the generation, propagation, and transformation of infragravity waves (IG) [4].

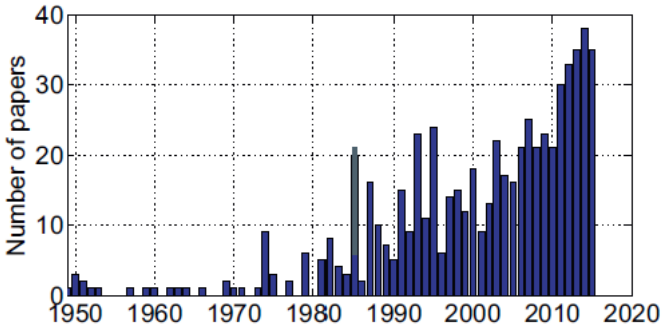

Figure 5: Number of papers per year found in Scopus and Web of Science where the title includes IG waves or surf-beat. (Bertin et al 2018).

Infragravity waves (IG) are surface ocean waves with frequencies below those of wind-generated “short waves”. Typical short-wave frequencies are between 0.04 and 1 Hz whereas IG wave frequencies are generally defined as being between 0.004 and 0.04 Hz. For a given water depth, IG waves have longer wavelengths than short waves. The first observation of IG waves date back only to the middle of the 20th century Munk in 1948 [14] and two years later Tucker found a positive correlation between the wave height of the wave group and the infra-gravity wave [5].

IG waves have a great number of implications in the hydro-sedimentary dynamics of coastal areas. For example, they can modulate current velocities in rip channels and strongly influence cross-shore and longshore mixing [2].

On sandy beaches, IG can have a strong impact on the water table and associated groundwater flows. On gently sloping beaches and especially in storm conditions, IG waves can dominate cross-shore sediment transport, generally promoting offshore transport within the surf zone.

In storm conditions, IG waves can also induce overwash and ultimately promote dune erosion and barrier breakthrough.

In tidal inlets, IG waves can propagate into the back-barrier lagoon during the flood phase and induce large modulations of currents and sediment transport. Their effect seems to be smaller during the reflux phase, due to the blocking of counter currents, especially in shallow systems [2].

On coral and rocky reefs, IG waves can prevail over short waves and control the hydro-sedimentary dynamics on the flat reef and in the lagoon.[2] They are considered to be the source of background free oscillations of the solid earth, also referred to as "the hum of the Earth" [15]. This large range of implications probably explains the growing interest in IG waves over the last decade, as it is attested by the increasing volume of literature on the topic (Figure. 5).

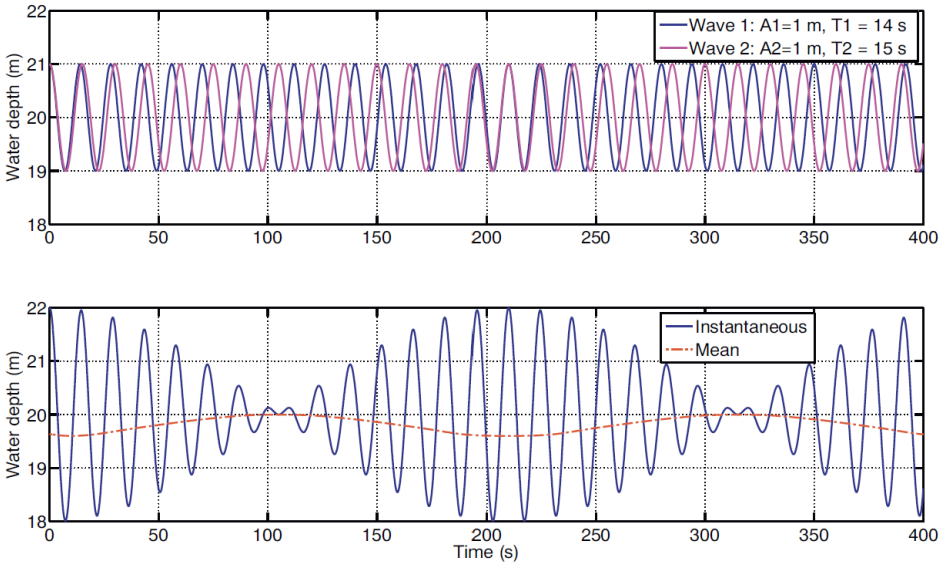

Figure 6: (A) Time series of two bichromatic waves with periods of 14 s (blue) and 15 s (pink) travelling over a flat bottom by 20 m water depth. (B) Resulting free surface elevation (blue) and bound wave (red). (Bertin et al 2018).

2 Methodology

To obtain a complete understanding of all the operations carried out throughout the experimental campaign, it is essential to provide an accurate description of their characteristics and the approach with which they were used. The different working instruments used have been explained below.

2.1 Instrumentation employed

The analyses were carried out in the wave channel of the Laboratory of Hydraulic and Maritime Constructions at the Polytechnic University of the Marche (Ancona). The channel has a rectangular cross-section (Figure 7) and is equipped upstream with a wave generator system (Figure 8). It is easily controlled by an on-site control unit.

The channel water supply and recirculation system are constructed with PVC pipes, which allow the height of the water to be adjusted to a predetermined level. A hydraulic system manages the filling of the channel and, if necessary, its emptying. The latter should be carried out to avoid water stagnation for prolonged periods or to allow detailed cleaning in preparation for an experiment. The dimensions of the canal are 1 meter wide and 50 meters long, with a height of 1.3 meters. The 36 meters long section of the canal is bordered on the sides by glazing. At the ends of the canal, where the wave generator system and an anti-reflective gravel beach are located, the side walls are closed and composed of metal panels.

The bottom of the channel consists of a 6 mm thick metal structure, which can optionally be covered with materials such as sand or plastic balls to replicate specific patterns for analysis.

Experiments were conducted in the central part of the channel. This area allows filming without visual obstacles and has a steel platform at the bottom with a straight section between two small ramps.

Figure 7: Channel.

Figure 8: Wave generator system.

2.2 Camera and lighting

Outside of the channel, in the previously mentioned area of interest, is a FLARE 12M125 CCD camera (Figure 9). This camera, with a resolution of 4100 X 3072 pixels and a pixel depth of 16 bits, is connected to a dedicated Express Core DVR. It stores all captured images, which are then transferred to the control computer. From the control computer, it is possible to start and stop recording, extracting the frames that are subsequently analysed during the post-processing stages.

Figure 9: FLARE 12M125 CCD camera.

A key step before capturing video is the focusing of the camera, followed by the evaluation of the pixel-to-meter conversion ratio. This step is crucial to determine how many meters a single pixel in the image corresponds to.

To perform this evaluation, a chessboard consisting of squares with a side of 2.5 cm is used, placed on a dedicated panel (see Figure 10).

The panel has been placed at different locations inside the field of view and several pictures of it have been taken with the camera. The goal of this process was to evaluate the dimension (in pixel) of a single chessboard square and, therefore, to estimate the pixel-to-mm ratio of the camera. The goal is to convert the displacements of the particles, measured in pixels, into measurable displacements in standard units.

A crucial aspect in improving the quality of the frames is to ensure adequate lighting. In the experiments conducted, it was vital to obtain the right brightness

in the lower part of the channel, focusing on a limited space instead of covering the entire width of the channel. To this end, an halogen lamp was used, firmly positioned above some steel beams that were resting on the upper edge of the channel, more or less 1m from the water surface, and appropriately configured to minimise light dispersion.

The strategic placement of the lamp prevented it from being reached by the waves once they had started.

The described setup of camera and lighting has been used to capture a series of images during the experiment of wave propagation. The pictures, called "frames", show an instantaneous capture of the position of seed particles that occurs at a specific time during the wave propagation process (monochromatic or bichromatic). The frames were acquired at a frame rate of 120fps, meaning that 120 frames were acquired for each second of recording.

Figure 10: Chessboard.

2.3 Seeding

Performing all laboratory tests, ground chili pepper was selected as the neutral substance. Its use involves tracking from the camera, which needs to be chemically and physically neutral to the water inside the channel as much as possible. This allows for an estimation of the velocity field during wave passage using the Particle Tracking Velocimetry (PTV) technique.

To gain an in-depth understanding of the methodology used, it is essential to start the exposition with the definition of the concepts of linear and Stokes theory. These concepts will provide the essential conceptual foundation for subsequent chapters, which will delve into the fluid and inertial behavior of a particle in detail.

2.4 Wave theory

In the next chapter, we refer to the procedure illustrated by P. K. Kundu, I. M. Cohen, and D. Dowling in the 2016 book "Fluid Mechanics 6th Edition".
We linearize the wave theory and find the Stokes drift.
Our coordinate system is two-dimensional where x is the horizontal direction and z the vertical. The depth is given by h and η is the free surface. The velocity field is defined as u (x, z, t) = (u,w), where u is the horizontal velocity and w is the vertical. The parameters used to define a wave are the amplitude a, the spatial frequency k, also called wave number, and the angular frequency ω. The wavelength λ is the distance from wave crest to crest and is defined as $\lambda = \frac{2\pi}{k}$. The period is denoted T and could also be defined as $T = \frac{2\pi}{\omega}$. The wave travels with phase speed $c = \frac{\omega}{k}$. β, which relates the fluid and particle densities, is evaluated with fluid density of 1000 kg/m^3 and particle density of 1050 kg/m^3, while the response time τ = 0.001s.
Note that later in the thesis we use the parameter Initial Phase = 3.6 and UU= 0.016 m/s which indicates the reverse current.

We start out the continuity equation

$$\frac{\partial \rho}{\partial t} + \nabla \cdot (\rho u) = 0 \tag{1.1}$$

Which states the principle of conversation of mass. We are only concerned about incompressible flow with constant density ρ, meaning the equation reduces to

$$\nabla \cdot u = 0. \tag{1.2}$$

The other equation describing describing a fluid is the Navier-Stokes momentum equation. For incompressible and inviscid flow, it is reduced to

$$\frac{Du}{Dt} = \frac{\partial u}{\partial t} + u \cdot \nabla \mathrm{u} = -\frac{\nabla \mathrm{p}}{\rho} + g \tag{1.3}$$

and named the Euler equation, which is a simplification of the Navier-Stokes momentum equation.

Lastly, we assume $\omega = \nabla \cdot \mathrm{u} = 0$ meaning the flow is irrotational. This makes it possible to define a velocity potential $\emptyset$:

$$\mathrm{u} = \nabla \emptyset. \tag{1.4}$$

Substituting the velocity potential into (1.2) leads to the Laplace's equation

$$\Delta \emptyset = 0. \tag{1.5}$$

The free surface problem has three boundary conditions. Two of the are kinematic boundary conditions and the last one is dynamic. The first one says that water cannot go through the bottom. This means that the normal velocity there has to be zero:

$$\omega = \partial \emptyset / \partial z = 0 \ \ on \ \ z = -h. \tag{1.6}$$

The second boundary condition says that the fluid particles at the free surface must have the same normal velocity as the normal velocity of the surface itself. This means that the fluid particles that make up the interface cannot leave the free surface and is written mathematically as

$$(\mathrm{n} \cdot u)_{z=\eta} = \mathrm{n} \cdot u_s \tag{1.7}$$

where n is the surface normal and u_s is the velocity of the free surface. The surface can be defined as f (x, z, t) = z - η(x, t) = 0. The normal surface is then defined as n = ∇f and using (1.7) leads to

$$\left(-u\frac{\partial\eta}{\partial x}+w\right)_{z=\eta}=\frac{\partial\eta}{\partial t}. \tag{1.8}$$

The boundary condition can also be written in terms of the velocity potential:

$$\left(-\frac{\partial\emptyset}{\partial x}\frac{\partial\eta}{\partial x}+\frac{\partial\emptyset}{\partial z}\right)_{z=\eta}=\frac{\partial\eta}{\partial t}. \tag{1.9}$$

It is assumed that the surface has a purely vertical velocity $u_s=\partial\eta/\partial te_z$.
For the last boundary condition, we need to re-write the Euler equation (1.3), into the Bernoulli equation:

$$\frac{\partial\emptyset}{\partial t}+\frac{1}{2}|\nabla\emptyset|^2+\frac{p}{\rho}+gz=0. \tag{1.10}$$

This is possible because the flow is irrotational, inviscid and incompressible. By saying that the pressure p just below the surface is the same pressure as p_0 just above, the Bernoulli equation is reduced to

$$\left(\frac{\partial\emptyset}{\partial t}+\frac{1}{2}|\nabla\emptyset|^2+gz\right)_{z=\eta}=0. \tag{1.11}$$

and we have the last boundary condition called the dynamic boundary conditions. To summarize, the partial derivatives are written in a more compact form and the free surface problem then looks like:

$$\begin{aligned}
&\emptyset_{xx}+\emptyset_{zz}=0 && \\
&\emptyset_z=0 && \text{on z } =-\text{h} \\
&\eta_t+\emptyset_x\eta_x-\emptyset_z=0 && on\ z=\eta \\
&\emptyset_t+\frac{1}{2}(\emptyset_x^2+\emptyset_z^2)+gn=0 && on\ z=\eta
\end{aligned} \tag{1.12}$$

2.5 Linear Theory

For waves with small amplitudes and slopes the problem can be linearized. The goal is to solve for the velocity potential ∅. It is assumed that the components u, w and η are all of the same order and higher order terms will then be neglected.

The kinematic boundary condition simplifies to:

$$\left(\frac{\partial \emptyset}{\partial z}\right)_{z=\eta} = \frac{\partial \eta}{\partial t}. \tag{1.13}$$

The left hand side is expanded around z = 0 leading to

$$\left(\frac{\partial \emptyset}{\partial z}\right)_{z=\eta} = \left(\frac{\partial \emptyset}{\partial z}\right)_{z=0} + \eta\left(\frac{\partial^2 \emptyset}{\partial z^2}\right)_{z=0} + \cdots \approx \frac{\partial \eta}{\partial t} \tag{1.14}$$

where the higher order terms are neglected and we are left with the linearized form of the kinematic boundary condition:

$$\left(\frac{\partial \emptyset}{\partial z}\right)_{z=0} = \frac{\partial \eta}{\partial t}. \tag{1.15}$$

The dynamic boundary condition (1.11) is simplified by dropping the non-linear terms and expanding around z=0. The linear condition then looks like this

$$\left(\frac{\partial \emptyset}{\partial z}\right)_{z=0} + g\eta = 0. \tag{1.16}$$

Since the free surface problem now is defined for the linear case, the velocity potential φ can be found. We assume that the wave takes the shape:

$$\eta(x,t) = a\cos(kx - \omega t). \tag{1.17}$$

Looking at the boundary conditions we see that the solution needs to be a sine function of phase (kx−ωt) for η to be correct. Therefore a solution is ”guessed” in the form of

$$\emptyset(x,z,t) = f(z)\sin(kx - \omega t) \tag{1.18}$$

where f(z) needs to be found. Substituting (1.18) into (1.5) leads to:

$$\frac{d^2 f}{dz^2} - k^2 f = 0 \tag{1.19}$$

which has the solution $f(z) = Ae^{kz} + Be^{-kz}$ where A and B are constants. The velocity potential becomes:

$$\emptyset(x, z, t) = Ae^{kz} + Be^{-kz} sin(kx - \omega t). \tag{1.20}$$

The constants are found by substituting (1.20) into the no flow trough condition (1.6):

$$k(Ae^{-kh} + Be^{kh}) \sin(kx - \omega t) = 0 \rightarrow \mathrm{B} = Ae^{-kh} \tag{1.21}$$

and using the kinematic boundary condition gives:

$$k(A - B) \sin(kx - \omega t) = \omega a \sin(kx - \omega t) \rightarrow \mathrm{K(A - B)} = \omega a. \tag{1.22}$$

The constants are then found to be:

$$A = \frac{a\omega}{k(1 - e^{-2kh})} \; and \; B = \frac{a\omega e^{-2kh}}{k(1 - e^{-2kh})} \tag{1.23}$$

and the velocity potential can then finally be defined as:

$$\emptyset(x, z, t) = \frac{a\omega}{k} \frac{\cosh(\mathrm{k(z + h)})}{\sinh(kh)} \sin(kx - \omega t). \tag{1.24}$$

The velocities in the x and z-direction then easy to find:

$$u\left(\frac{\partial \emptyset}{\partial x}\right) = a\omega \frac{\cosh(\mathrm{k(z + h)})}{\sinh(kh)} \cos(kx - \omega t). \tag{1.25}$$

$$w\left(\frac{\partial \emptyset}{\partial z}\right) = a\omega \frac{\sinh(\mathrm{k(z + h)})}{\sinh(kh)} \sin(kx - \omega t). \tag{1.26}$$

Until now, the dynamic boundary condition has not been used. Inserting $\emptyset$ and η into (1.11) produces

$$-\frac{\mathrm{a}\omega^2}{k}\frac{\cosh(\mathrm{kh})}{\sinh(kh)}\cos(kx-\omega\mathrm{t}) = -\mathrm{ga}\ \cos(kx-\omega\mathrm{t}) \qquad (1.27)$$

which simplifies to what is called the dispersion relation:

$$\omega = \sqrt{gk\ \tanh\ (kh)}. \qquad (1.28)$$

The dispersion relation explains how the temporal and spatial frequency are connected. Since the phase speed of the waves is given by c = ω/k it can by using this relation be written

$$\mathrm{c} = \sqrt{\frac{g}{k}\tanh(kh)\ } = \sqrt{\frac{g\lambda}{k}\tanh(\frac{2\pi h}{\lambda})}\,. \qquad (1.29)$$

Waves with larger wavelength λ will then travel faster compared to shorter waves.

2.6 Stokes Drift

For the linearized particle paths, particle motion follows closed circles or ellipses. The mean velocity of a particle will then be zero. However, in a real-life situation, if something is thrown into the ocean, it will slowly drift in the direction of propagation. Thus the mean velocity is not zero and this slow movement is called Stokes drift. By keeping higher order terms in the Taylor series of the velocity of the particle

$$\frac{dx}{dt} = u(x,z,t) = u(x_0,z_0,t) + (x-x_0)\left(\frac{\partial \mathrm{u}}{\partial \mathrm{x}}\right)_{xo,zo} + (z-z_0)\left(\frac{\partial \mathrm{u}}{\partial \mathrm{x}}\right)_{xo,zo} + \ldots \qquad (1.30)$$

$$\frac{dz}{dt} = w(x,z,t) = w(x_0,z_0,t) + (x-x_0)\left(\frac{\partial \mathrm{u}}{\partial \mathrm{x}}\right)_{xo,zo} + (z-z_0)\left(\frac{\partial \mathrm{u}}{\partial \mathrm{z}}\right)_{xo,zo} + \ldots, \qquad (1.31)$$

the Stokes drift can be obtained. The position (x0; z0) is the fluid's location if there was no waves. The velocities are defined in (1.25) and (1.26). The horizontal and vertical distances in the Taylor series are defined like

$$x - x_0 = \int_0^t u(x_0,z_0,t')dt' = \ \ldots \qquad (1.32)$$

$$-a\frac{\cosh(\mathrm{k}(z_0+\mathrm{h}))}{\sinh(kh)}\sin(kx_0-\omega\mathrm{t}) \qquad (1.33)$$

$$z - z_0 = \int_0^t w(x_0, z_0, t')dt' = \ \ldots \tag{1.34}$$

$$-a\frac{\sinh(\mathrm{k}(z_0+\mathrm{h}))}{\sinh(kh)}\cos(kx_0 - \omega\mathrm{t}). \tag{1.35}$$

Integrating (1.30) and (1.31) over a period T and then dividing by T, the time averages are found:

$$u_s = a^2\omega k\frac{\cosh(2\mathrm{k}(z_0+\mathrm{h}))}{2sinh^2(kh)} \tag{1.36}$$

$$w_s = 0 \tag{1.37}$$

As seen, there is no Stokes drift in the vertical direction. As the particles moves in the direction of wave propagation, it causes mass transport. Another word for Stokes drift is mass transport velocity. The Stokes drift is also the difference between Eulerian and Lagrangian velocity [12]:

$$\text{Stokes drift} = V_L - V_E$$

Everything is calculated using MATLAB which allowed us to quickly analyse data and perform calculations.

The suite used to perform particle tracking is Part2Track, which uses the Particle Tracking Velocimetry (PTV) approach and is capable of handling image sets on which it performs particle tracking. It takes advantage of the Matlab development framework and allows for both pre- and post-processing operations. Originally, PTV has solely been used for the evaluation of sparsely seeded flows. But over the time, PTV algorithms with the ability to handle large amounts of particles have been developed. Whereas early PTV studies have primarily been used to analyze time resolved image series, recent approaches extended the method to cope with double frame image data as well. [7]

The analyses done and the various image processing steps are described below.

2.7 Pre-Processing

Initially, we imported the folder named "raw" containing all the frames to be analysed, the "Part2track" folder, and the script "Parameter.m" into Matlab which will be explained in the following chapters. Even before removing the background and adjusting the contrast, we had to run the "FrameRenumber" script for the numbering of the frames to be analyzed, so that they start from 0001 and go in ascending order. It is suggested to use this approach when the frames to be processed are extracted from the central part of a video for which the frames have numbering that does not start from 0001. The second code to be used, called RemoveBackground.m, allows any noise and non-particle objects to be removed. This is required since the Part2Track software needs to work with clean, dark background images. The number of frames in the 'raw' folder to be analyzed is set, also specifying the number of frames to be averaged over for the identification of background features to be removed by RemoveBackground.m.

The routine is executed only for the first few frames, those obtained by subtracting the number of frames on which to average from the number of frames to be analyzed. So, once the number of frames to average over has been identified, the RemoveBackround.m script works on this amount of images starting with the first one in the 'raw' folder. Having determined the average backround of these frames, it is removed from all the images. Once the script is run, a 'noBack' folder is generated, containing all the frames folder with no background.

If we compare the figures 11 and 12, we can see the clear difference from the initial frame (Figure 12) to the one after running the script RemoveBackround.m (Figure 11). In the second one the turbidity region appearing in the bottom part of the unaltered frame has been removed through the background removal process.

To make the particles more visible to the software, it is also necessary to increase the contrast of the images. The script that allows this to be done is known as AdjustContrast.m. The images are now no longer taken from the initial 'raw' folder, but from 'noBack', the result of the previous step performed by removing the background. By running this script, you can manually adjust the new intensity

limits to achieve the desired contrast. The right trade-off is to observe brighter, visible particles while at the same time adding further unwanted noise. Once the 'Minimum' and 'Maximum' limits of the desired intensity have been identified, the same brightness limits are applied to all the frames contained into the "NoBack" folder, and the resulting images are collected in a new 'contrast' folder. This then contains all the frames for which the background has been removed and the contrast corrected (see Figure 13).

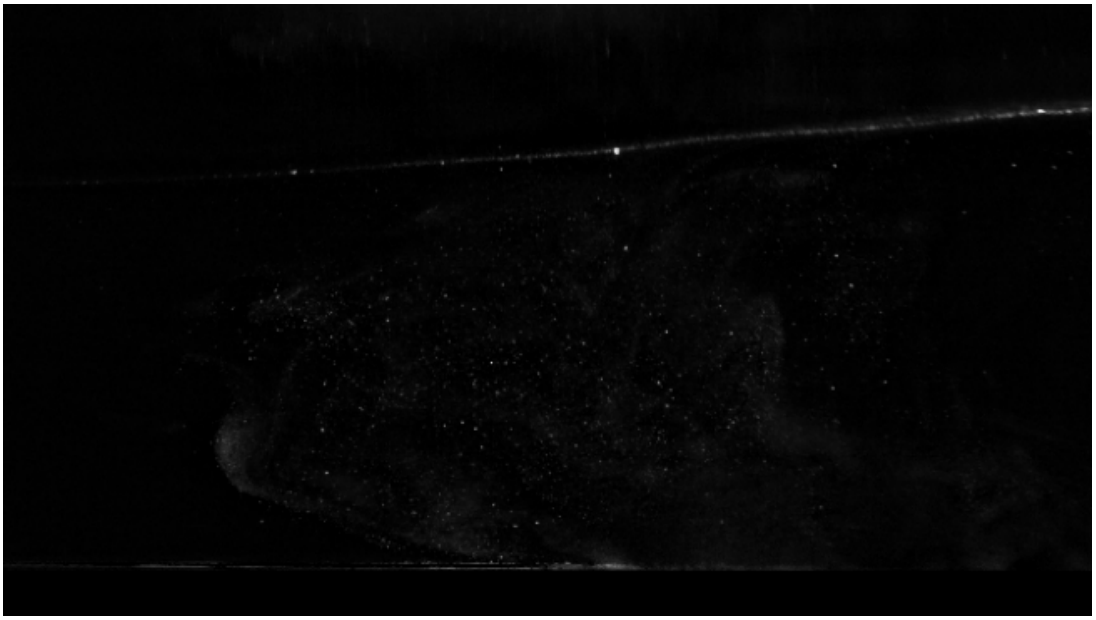

Figure 11: Frame with the background.

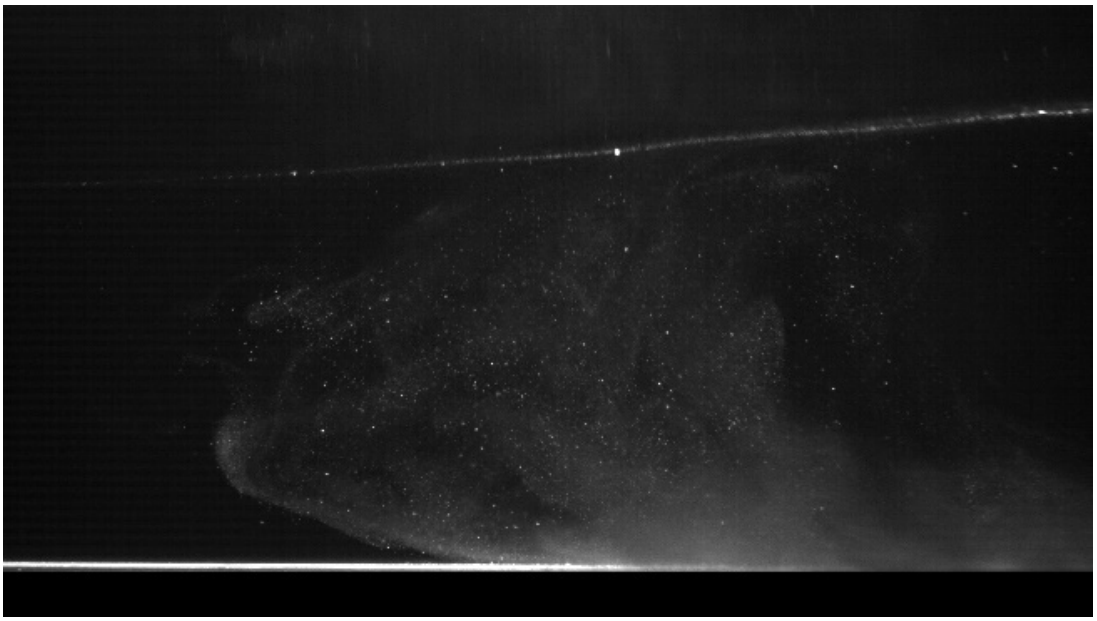

Figure 12: Frame without background.

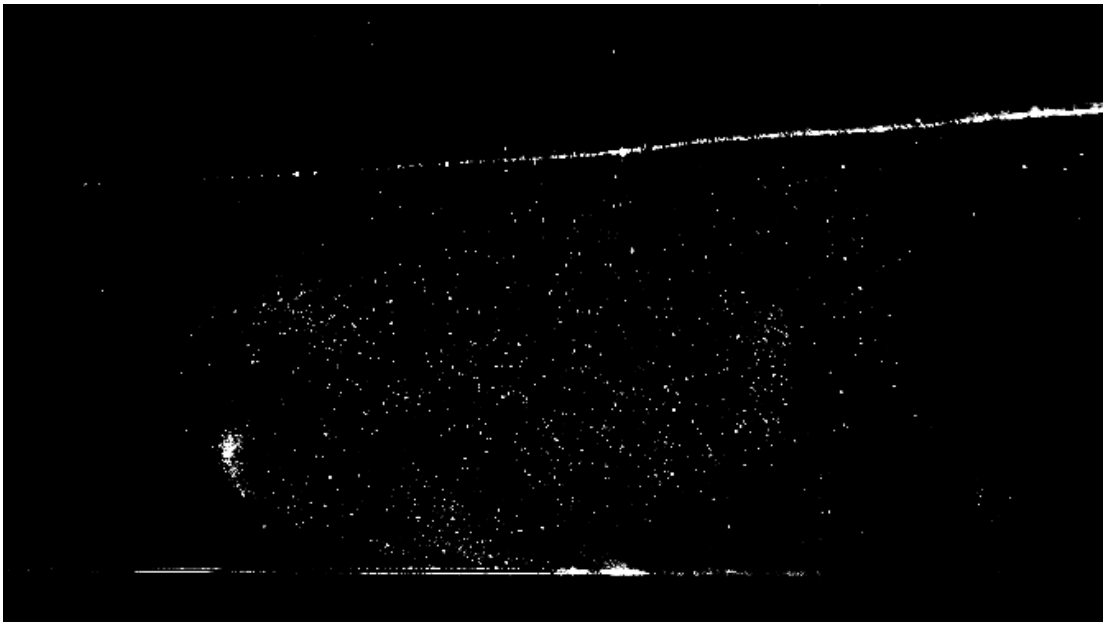

Figure 13: Frame with contrast.

2.8 Post-Processing

The post-processing, which consists of the proper tracing of particles from frames, is based on the parameter file called parameter.m, which contains a number of very important parameters. The first of these, denoted as 'im_res' represents the resolution of the camera used. Specifically, the two numbers written describe the height and width of the frame, respectively. The time step between two consecutive frames is denoted as 'dt', which is nothing more than the inverse of framerate.

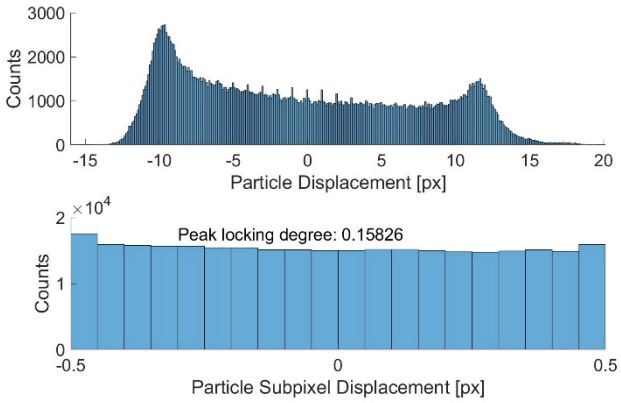

Figure 14: Particle Displacement[px].

The two parameters that govern the process of particle recognition within frames are 'p_size' and 'p_int'. The first one indicates the average particle size in pixels, with typical values of 9,11 and 13 identified by thorough analysis while the second one is the average particle intensity always expressed in pixels. After a series of analysis, it was chosen 7000 as the value of p_int.

The main Matlab code for particle tracking is placed inside the 'src' folder, contained in the Part2Track software, and is called main_proc.m. It takes as input images those within the 'contrast' folder, while the output comes in the form of another folder 'results'. Particle detection is performed by tracking particles, which appear in consecutive frames and by estimating their displacement and velocity. By reviewing each frame, particle trajectories are then extracted, the displacement of which is provided in pixels in the form of histograms (see Figure 14). The most important result, however, is a graph from which emerge, in various colours, all

the orbital paths traced by the particles. Most of them are not perfectly close because the traced particles seldomly disappear from the frames due to them moving outside of the light sheet following the wave motion, which can lose sight of a certain particle by moving from one frame to the next. Figure 15 represents the average velocity field and the trajectories of the particles.

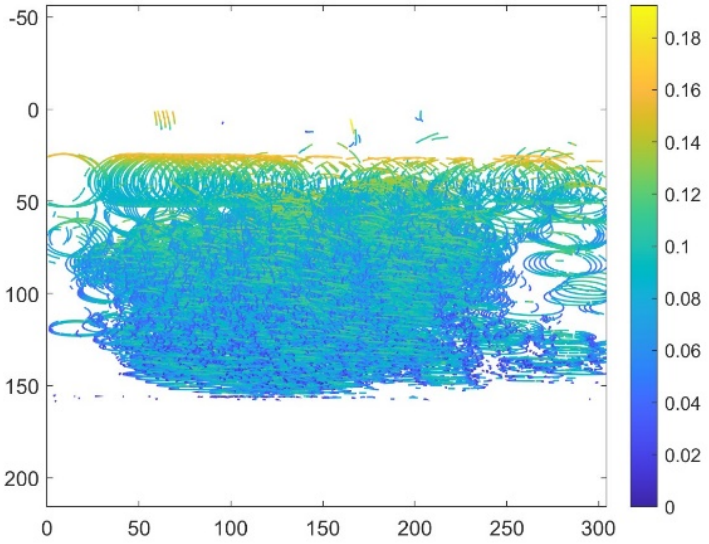

Figure 15: Velocity and trajectories of the particles.

Then, a video was generated using the script called "VectorFieldVideo.m," in which we can observe the velocity field of the detected particles.

In Figure 16 a snapshot of the particle velocity field generated in response to the passage of the wave is shown. The cloud of particles is seen to clearly move to the left part of the frame as a wave trough is moving from the left to the right.

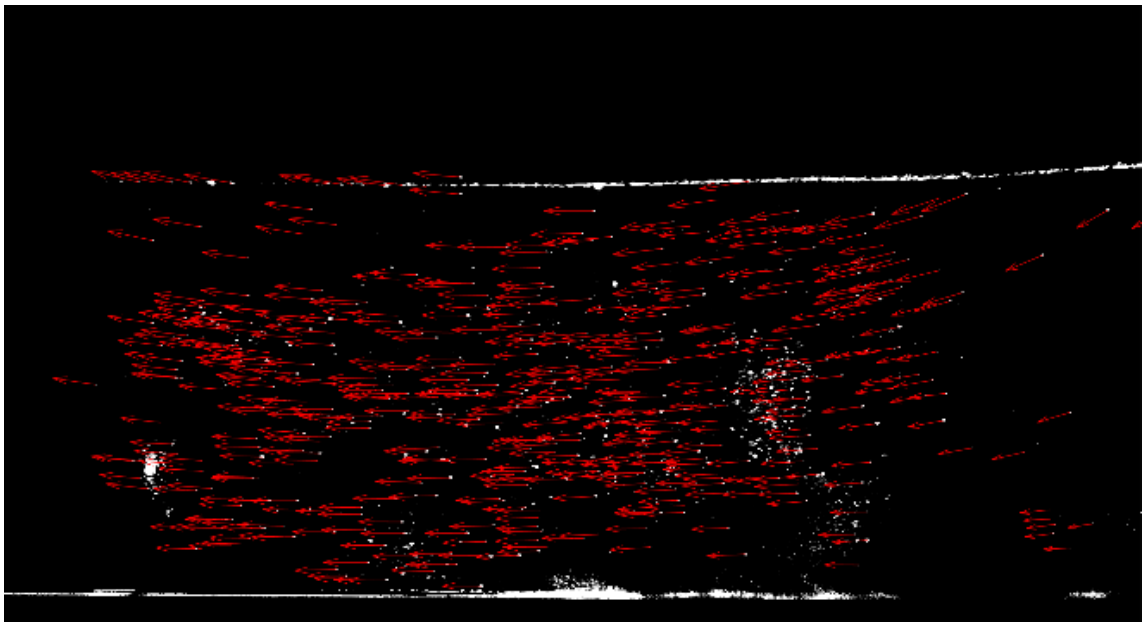

Figure 16: Vector field.

It is easy to see how in the central part of the wave, there is good seeding throughout the water column, which allowed us to obtain a fairly robust analysis.
The next Matlab code is called VectorFieldInterpolate.m. This script allows the user to interpolate the velocity field extrapolated by Part2Track, which is configured as a set of dispersed vectors, over a regular grid defined by a specific number of points in the x- and y-direction (mm). The larger the size of such a grid, the larger the discretization in both directions. In our case we created a grid composed of 400 columns and 300 rows.
Velocity profiles at any given vertical column in the field of view can be obtained using the script "VelocityFieldPhaseMean.m" for those averaged in phase. In particular, it is possible to choose a specific vertical line from which velocity profiles are extracted. In our case, the chosen "ixprofile" is 170 because, knowing that the grid consists of 400 columns and the area with more particles is just before the central part of the wave, we chose a value that referred to that area. "VelocityFieldPhaseMean.m" analyzes the velocity fields corresponding to the same phase across consecutive wave cycles are then grouped and averaged. In this

way, an indication of how the velocity profile across the water column varies according to the wave phase (i.e. across a wave cycle) can be obtained.
The graph obtained is shown in Figure 17. Observing the values taken by "u" along the x-axis, it can be seen that the velocity profile oscillated between a maximum of 0.1 m/s and a minimum of -0.1 m/s, with the negative value indicating particle movement in the opposite direction to the wave propagation. Instead, with "VelocityFieldPeriodMean.m," it is possible to obtain velocity fields again, but this time averaged over the period. This means that the procedure is almost identical to the previous one, but in this case, all velocity fields falling within a single wave period, i.e. between two correspondent wave phases, are grouped and averaged. Here, the "ixprofile" we chose is the same of before (170). The graph obtained from this procedure is illustrated in Figure 18 where in the x-axis we have the horizontal component “u” and the y-axis shows the vertical distance measured from the top in mm. The various profiles are associated with the quadratic error of the mean profile with respect to all vertical profiles,of the horizontal velocity “u” ,used to obtain it. These results refer to a monochromatic wave, later these considerations will also be made for the bichromatic one.

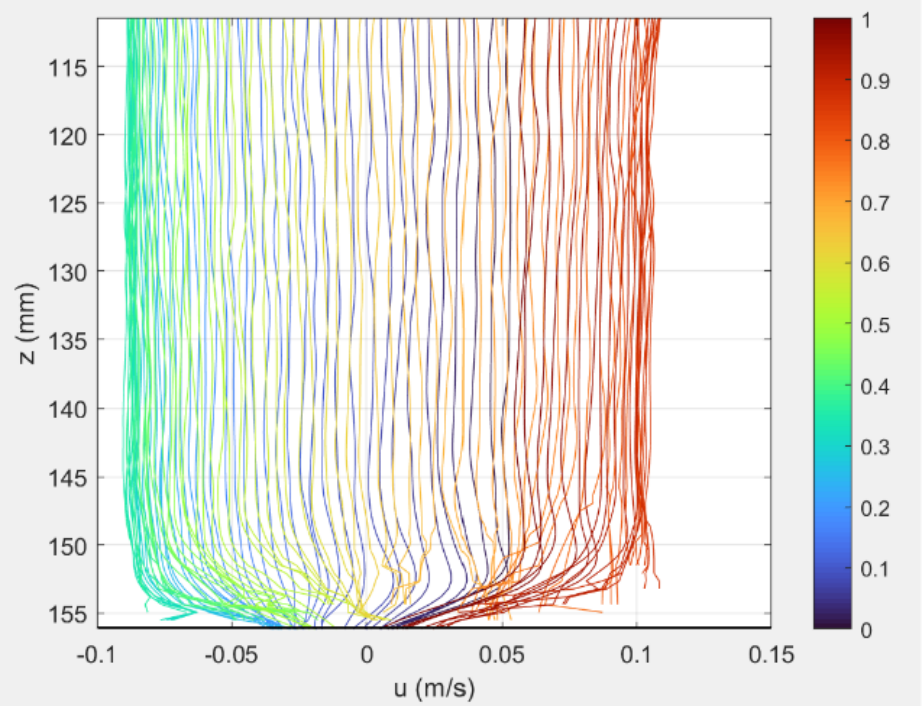

Figure 17: Phase mean.

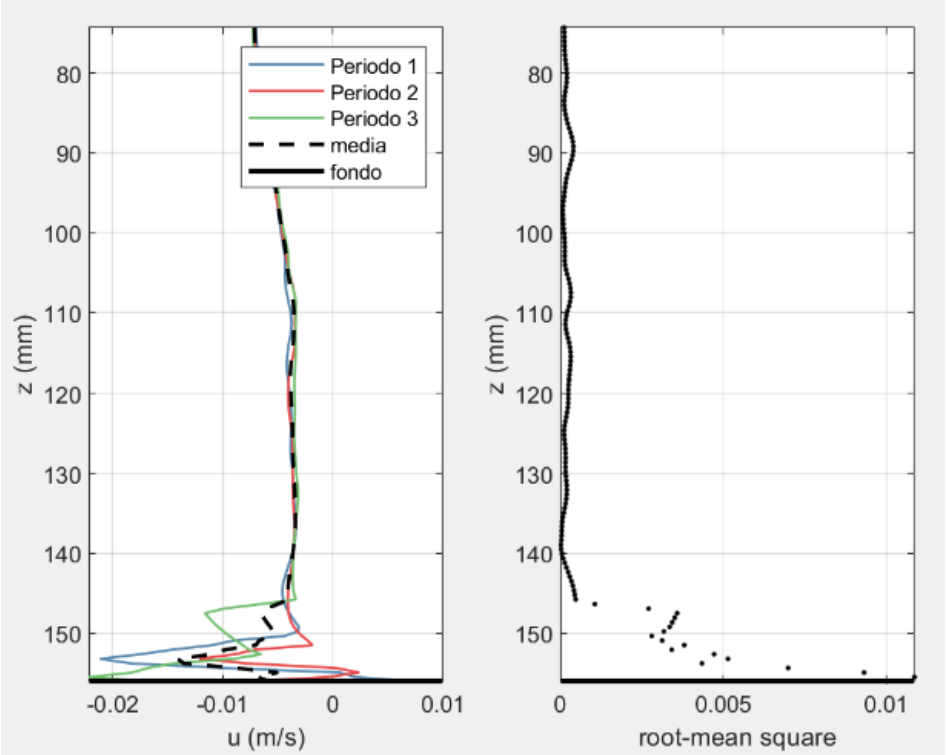

Figure 18: Period mean.

3 Results

3.1 Analysis of Monochromatic Waves

Through the script 'LongestTrajectories.m', we were able to plot the trajectories of particles. With this tool, we were able to select the frame to be analysed and the number of trajectories to be plotted by Matlab. To ensure clearer and faster results, we configured Matlab to show only the longest trajectories.

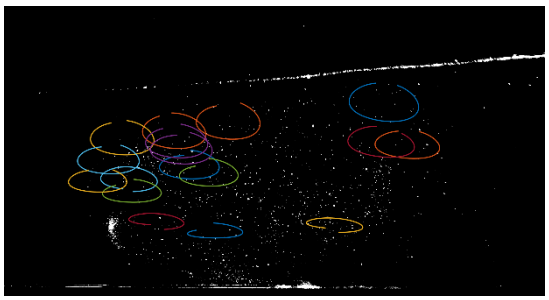

Figure 19: Incomplete Trajectories.

Initially, we performed a visual analysis of the trajectories. Some of them were discarded because they were incomplete, as shown in Figure 19. This was mainly caused by Matlab's difficulty in tracking the motion of some particles during data acquisition. On the contrary, some trajectories, such as the one illustrated in Figure 20, showed a pattern that led the particle towards the free surface, or towards the bottom of the channel as shown in Figure 21.

This phenomenon can be attributed to the fact that the frames are related to approximately a few minutes after the release of the seeding, therefore it was predictable that they had stabilized in terms of falling speed.

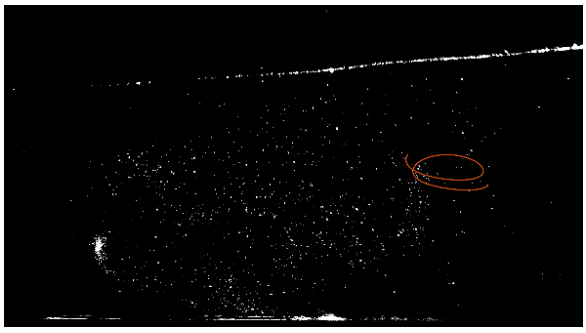

Figure 20: Rising Trajectory.

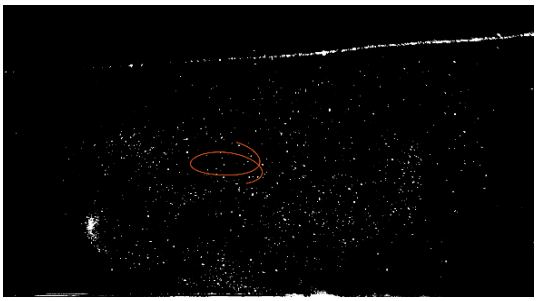

Figure 21: Sinking Trajectory.

After an in-depth analysis, it turned out that by setting the parameter p-size (Particle size in px) to 13 and options.min_dist (Maximum deviation from position prediction in px) to 5, Matlab was able to plot more precise and longer trajectories, as seen in Figure 22. Next, we identified twenty-two trajectories that we considered optimal through visual observation. For each of these trajectories, we calculated the maximum and minimum with respect to the x and y axes.

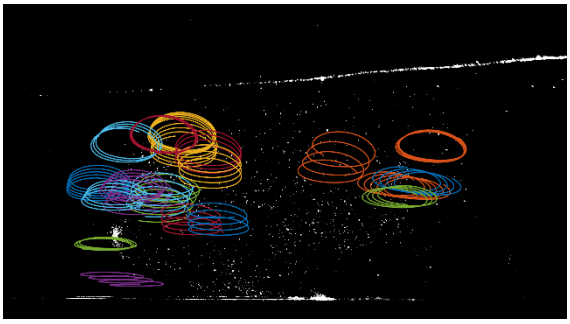

Figure 22: Trajectories.

The resulting graphs, similar to those presented in Figures 23 and 24, delineate the maximum and minimum with respect to the x-axis in the first graph and with respect to the y-axis in the second.

By analysing these graphs and the trajectory section in the frame, it was also possible to identify different types of trajectories. In the previously selected trajectories, there were trajectories with a positive trend (heading towards the wave direction), trajectories with a negative trend (moving in the direction opposite to the wave direction) and trajectories characterised by a sinking trend. The latter, in turn, were further subdivided into negative and positive trajectories.

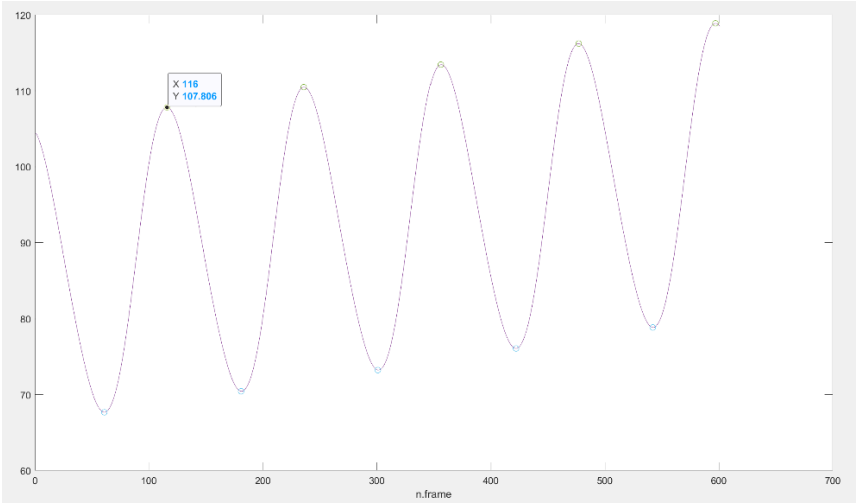

Figure 23: Maxima and minima along the x-axis.

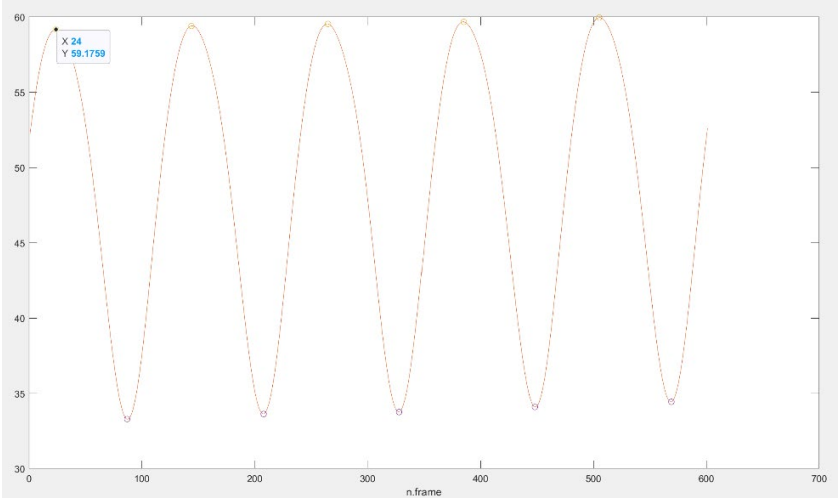

Figure 24: Maxima and minima along the y-axis.

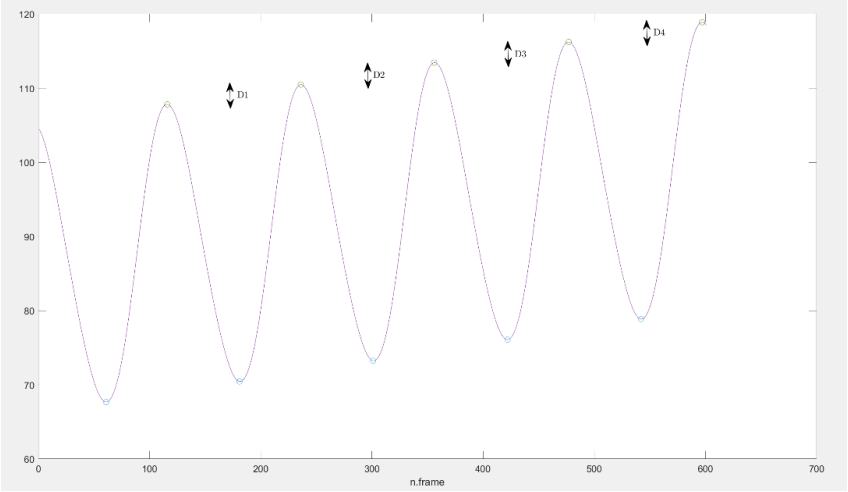

Figure 25: Difference between maxima and minima on the x-axis.

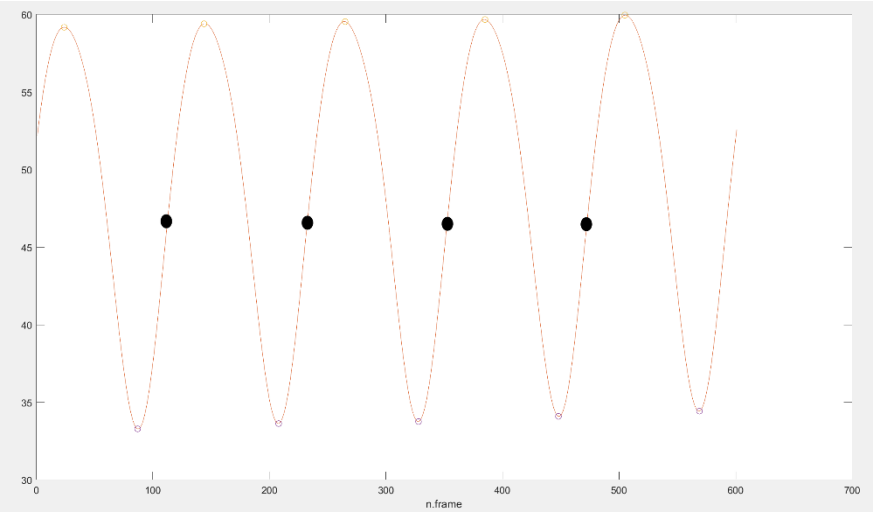

Figure 26: Midpoint between maxima and minima on the y-axis.

Now, our objective was to analyze the Horizontal Drift (Dx), taking into account the position and direction of each trajectory with respect to the wave. The Dx was calculated as the difference between two maxima or two minima from the values obtained on the x-axis (Figure 25). After calculating these differences for each trajectory, we added them up to obtain an average. As for the position and direction of the trajectory with respect to the wave, we calculated the midpoint between a maximun and a minimum of the values obtained on the vertical axis, as shown in Figure 26, and then calculated the average.

We then represented these values in a graph, in which the Horizontal Drift was entered on the x-axis and the Y values obtained on the y-axis (Figure 27). It illustrates the behaviour of the Horizontal Drift in relation to depth and only particles moving in the same direction as the wave and those moving in the opposite direction have been portrayed.

It is evident that negative values correspond to negative trajectories and positive values to positive trajectories. The light blue line represents the free surface while the dark blue line represents the channel bed.

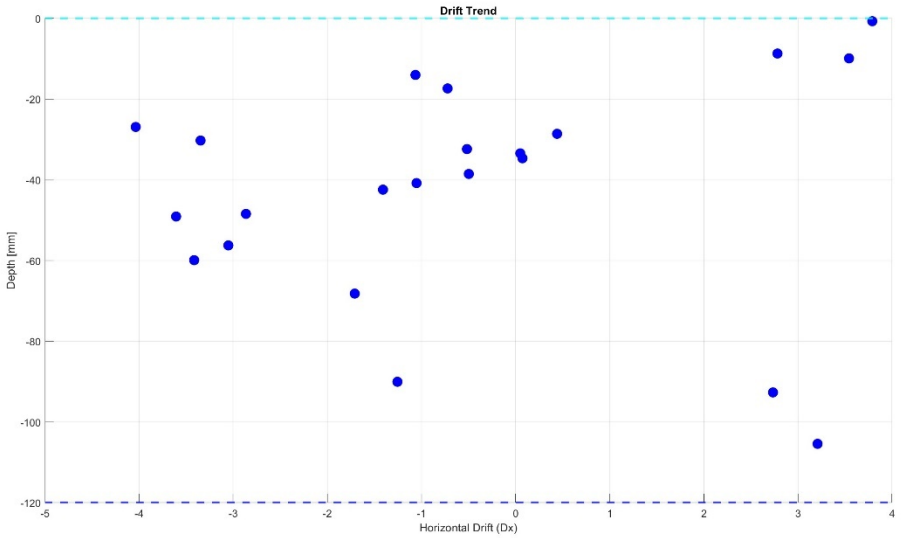

Figure 27: Horizontal Drift (Dx).

Knowing that the camera used has captured 120 frames per second, the Drift velocities (U_L) can be calculated as follows. After determining the number of frames for each maximum or minimum recorded along the x-axis, we obtained the time associated with each point of maximum and minimum for each trajectory.

Next, we calculated the Lagrangian period (T_L) where $T_1, T_2..$, corresponds to x values calculated along the x-axis (see Figure 23)

$$T_L = \frac{[|(T_1 - T_{2)}| + |(T_2 - T_3)| + |(T_3 - T_4)| \dots]}{n} \; x \; \frac{1}{120}$$

Finally, we have that (U_L) is obtained by the following formula

$$U_L = \frac{Dx}{T_L}$$

The figure 28 illustrates the drift velocity trend as a function of depth, showing a remarkable similarity to the horizontal drift trend,as expected. This consistency is attributed to the fact that the Lagrangian period remained consistently close to 1 second. This result confirms the reliability of our data, considering that the camera is capable of capturing 120 frames per second.

To differentiate one trajectory from another, a reference number has been assigned and is also reported in the graph (Figure 28).

Visual analysis of the Drift velocities clearly suggests an ideal best-fit curve.

However, four trajectories near the free surface appeared anomalous, initially considered as extreme values. Further analysis revealed that these trajectories behaved as fluid, not as inertial particles. As a result, it turned out that the fitting curve should pass through those particles as well. To distinguish whether the particles at hand were fluid or inertial, two distinct scripts have been used based on both linear theory and Stokes theory.

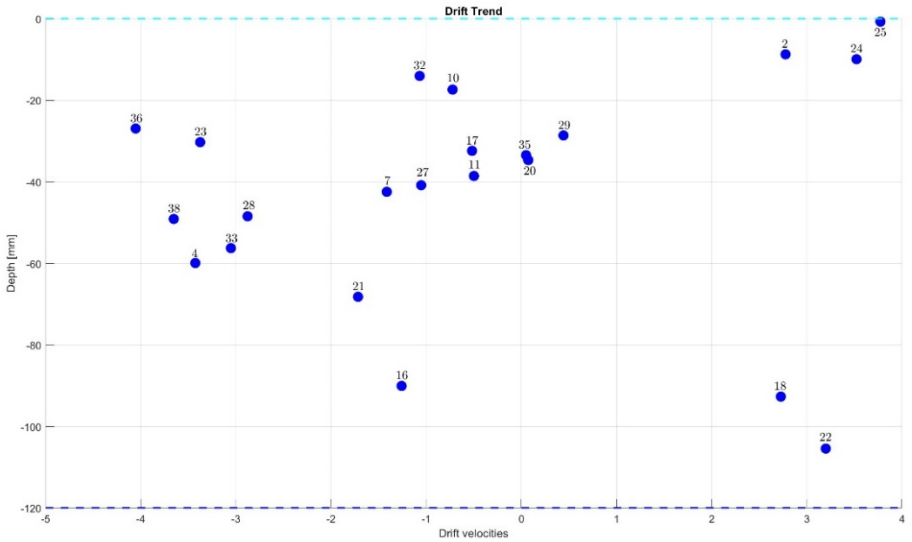

Figure 28: Drift velocities.

c

3.2 Fluid particle motion

The single particles of the fluid are considered an integral part of the total fluid mass. They follow the flow, and their speed is essentially the same as that of the fluid.

To identify whether a particle exhibited behavior similar to that of a fluid particle, a Matlab script was used to trace both the real trajectory considered (real path) and the trajectory modeled by solving the following equations (linear theory):

$$u\left(\frac{\partial \emptyset}{\partial x}\right) = \mathrm{a}\omega\ \frac{\cosh\left(\mathrm{k}(\mathrm{z}+\mathrm{h})\right)}{\sinh\left(kh\right)}\cos(kx - \omega\mathrm{t} + \mathrm{phase}) - \mathrm{UU},$$

$$w\left(\frac{\partial \emptyset}{\partial z}\right) = \mathrm{a}\omega\ \frac{\sinh\left(\mathrm{k}(\mathrm{z}+\mathrm{h})\right)}{\sinh\left(kh\right)}\cos(kx - \omega\mathrm{t} + \mathrm{phase})$$

and also, an additional comparison of the velocity field of a Stokes wave, defined by equations (1)-(2) in Boffetta et al (2013) [12].

$$u\ = \mathrm{U}\ \frac{\cosh\left[\mathrm{k}(\mathrm{z}+\mathrm{h})\right]}{\sinh\left(kh\right)}\cos(kx - \omega\mathrm{t}) + \frac{3U^2}{4c}\frac{\cosh\left[2\mathrm{k}(\mathrm{z}+\mathrm{h})\right]}{\sinh^4(kh)}\cos[2(kx - \omega\mathrm{t})] - \mathrm{UU}, \quad (1)$$

$$w\ = \mathrm{U}\ \frac{\sinh\left[\mathrm{k}(\mathrm{z}+\mathrm{h})\right]}{\sinh\left(kh\right)}\sin(kx - \omega\mathrm{t}) + \frac{3U^2}{4c}\frac{\sinh\left[2\mathrm{k}(\mathrm{z}+\mathrm{h})\right]}{\sinh^4(kh)}\sin[2(kx - \omega\mathrm{t})]. \quad (2)$$

3.3 Inertial particle motion

The inertial particles are solid or liquid and are suspended in the fluid. They have sufficient mass to resist the viscous forces of the fluid. They can have independent trajectories and can be influenced by inertial forces. To determine if a particle displayed characteristics resembling those of an inertial particle, a Matlab script has been employed, which deals with solving the set of equations (3)-(4) present in the study by Boffetta et al. (2013) [11], where x(t) and **V**(t) represent, respectively, the particle position and its velocity. In (4) the Stokes response time is τ where a is the particle radius and v the kinematic viscosity of the fluid, and the added-mass effect has been taken into account via the dimensionless number β, built from the fluid, ρ_f , and particle, ρ_p, densities

$$\frac{dx}{dt} = \boldsymbol{V} \tag{3}$$

$$\frac{d\mathbf{V}}{dt} = \frac{u-\mathbf{V}}{\tau} + (1-\beta)g + \beta\frac{du}{dt} \quad , \quad \beta = 3\rho_f/(\rho_f + 2\rho_p) \ , \ \tau = a^2/(3\beta_v) \tag{4}$$

using as initial conditions the position and velocity of the particle, which we have estimated from the trajectory data. The script used the orbital velocity field of a harmonic wave as per the classic linear wave theory, and an additional comparison of the velocity field of a Stokes wave, defined by equations (1)-(2) in Boffetta et al (2013) as for fluid particles.

$$\mathrm{u} = \mathrm{U}\frac{\cosh\,[\mathrm{k(z+h)}]}{\sinh\,(\mathrm{kh})}\cos(\mathrm{kx}\text{-}\,\omega\mathrm{t}) + \frac{3\mathrm{U}^2}{4\mathrm{c}}\frac{\cosh\,[2\mathrm{k(z+h)}]}{\sinh^4(\mathrm{kh})}\cos[2(\mathrm{kx}\text{-}\omega\mathrm{t})]$$

$$\mathrm{w} = \mathrm{U}\frac{\sinh\,[\mathrm{k(z+h)}]}{\sinh\,(\mathrm{kh})}\sin(\mathrm{kx}-\omega\mathrm{t}) + \frac{3\mathrm{U}^2}{4\mathrm{c}}\frac{\sinh\,[2\mathrm{k(z+h)}]}{\sinh^4(\mathrm{kh})}\sin[2(\mathrm{kx}-\omega\mathrm{t})].$$

A comparison was made between the trajectories considered "anomalous" and those slightly below, belonging to the rest of the group. 36,23,32 and 10

trajectories have been analyzed in comparison to trajectories 7, 27, 11 and 17. The choice of trajectories 7, 27, 11 and 17 derived from the fact that they were all negative paths (i.e. they move in the opposite direction to the propagation of the wave), they were located at approximately the same depth and had a similar horizontal drift. For the script regarding the recognition of inertial behaviour, it is essential to know the radius of the particle.

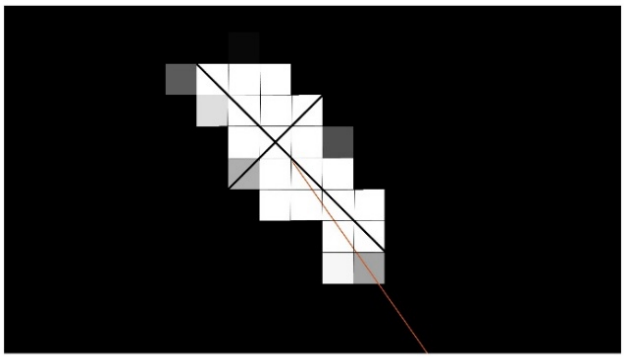

Figure 29: snapshot for estimating the particle size relative to the trajectory 36.

As can be seen in equation (4) the particle radius is fundamental for the calculation of τ. Given the absence of particles with a uniform shape, it was necessary to initially divide the area of the particle analyzed into numerous small squares, each corresponding to a single pixel. Next, the radius of the particle was calculated by averaging between the major and minor diameters, as shown in Figure 29.

The conversion from pixels to millimeters was performed by multiplying the number of pixels by the conversion factor specified in the parameter.m script: $\frac{27}{\text{average}([363.0675,364.3968,362.4045])}$.

The trajectories analyzed are shown in the table below.

n.Trajectories	Depth [mm]	D[mm]	d[mm]	Particle radius [mm]	Particle radius [m]
23	30,251	0,520246107	0,222962617	0,371604362	0,000371604
36	26,8952	0,520246107	0,222962617	0,371604362	0,000371604
7	42,4291	0,594566979	0,371604362	0,48308567	0,000483086
27	40,8056	0,445925234	0,222962617	0,334443926	0,000334444
11	38,5365	0,520246107	0,222962617	0,371604362	0,000371604
17	32,3692	0,668887851	0,371604362	0,520246107	0,000520246
32	14,0009	0,520246107	0,222962617	0,371604362	0,000371604
10	17,348	0,594566979	0,29728349	0,445925234	0,000445925

Table 1: Characteristics of the trajectories analyzed.

As previously mentioned in the script used for fluid particles, we generated two graphs for each trajectory. The ones on the left (Figs. 30, 32..) are calculated by applying the linear theory, while the ones on the right is based on Stokes theory.

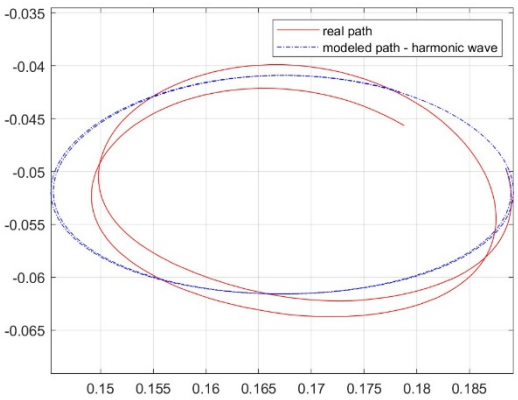

Figure 30: Trajectory 32, Fluid particle-Linear theory.

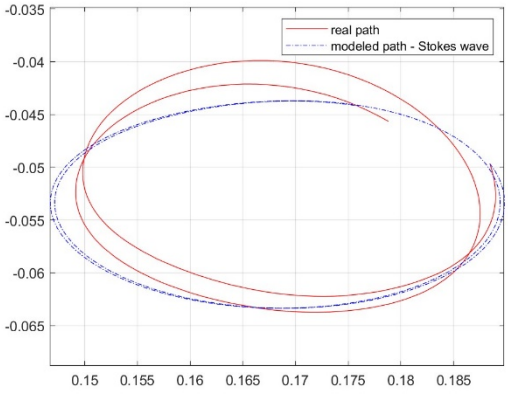

Figure 31: Trajectory 32, Fluid particle-Stokes theory.

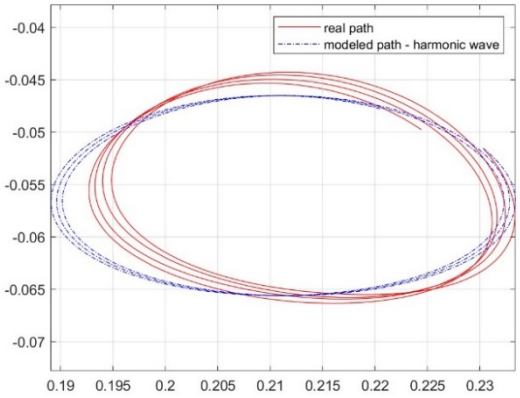

Figure 32: Trajectory 10, Fluid particle-Linear theory.

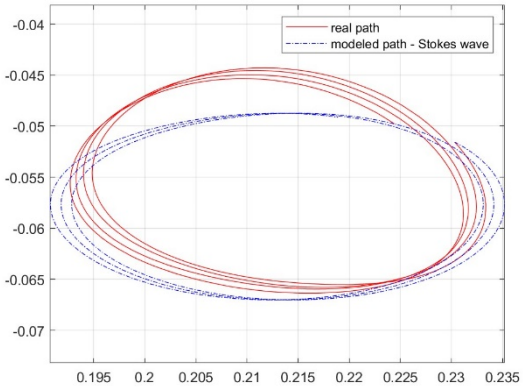

Figure 33: Trajectory 10, Fluid particle-Stokes theory.

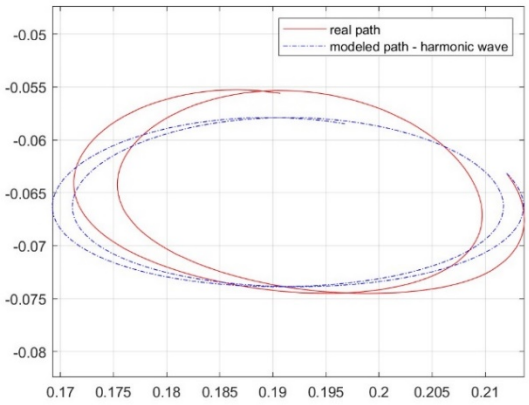

Figure 34: Trajectory 36, Fluid particle-Linear theory.

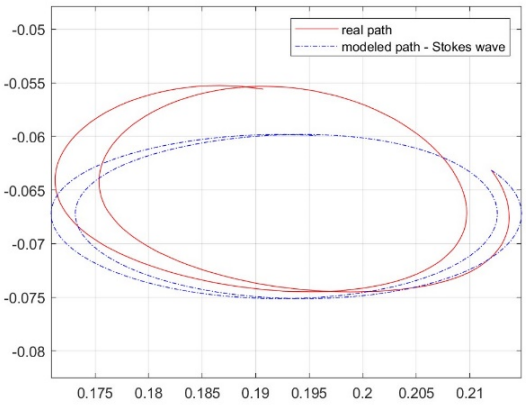

Figure 35: Trajectory 36, Fluid particle-Stokes theory.

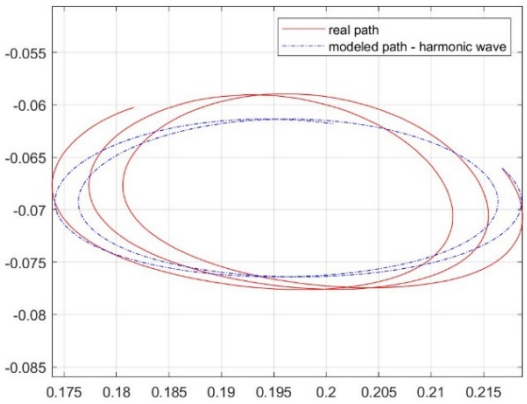

Figure 36: Trajectory 23, Fluid particle-linear theory.

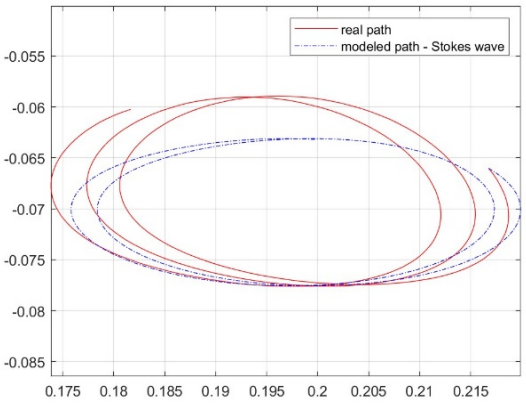

Figure 37: Trajectory 23, Fluid particle-Stokes theory.

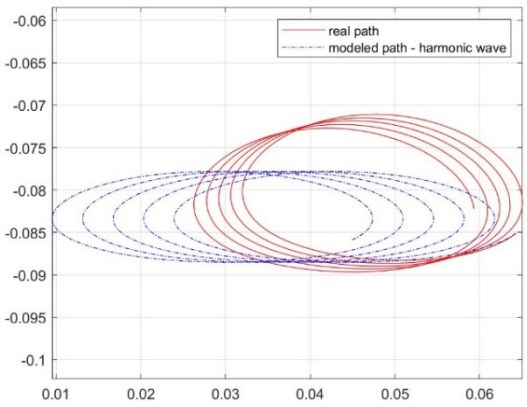

Figure 38: Trajectory 7, Fluid particle-linear theory.

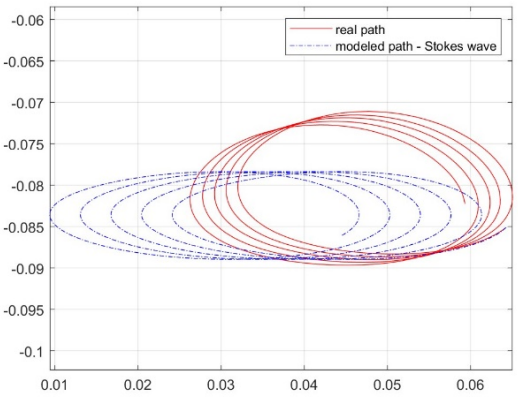

Figure 39: Trajectory 7, Fluid particle-Stokes theory

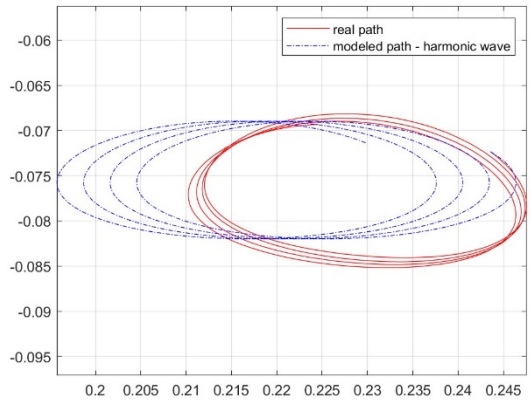

Figure 40: Trajectory 11, Fluid particle-linear theory.

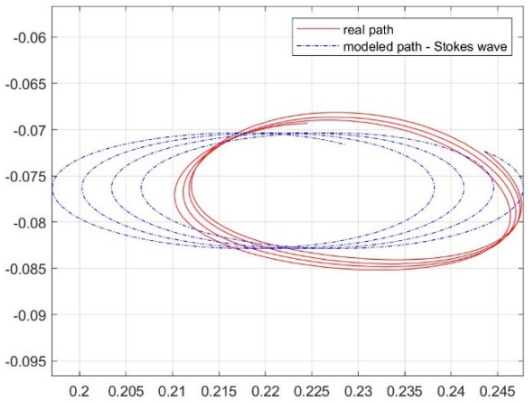

Figure 41: Trajectory 11, Fluid particle-Stokes theory.

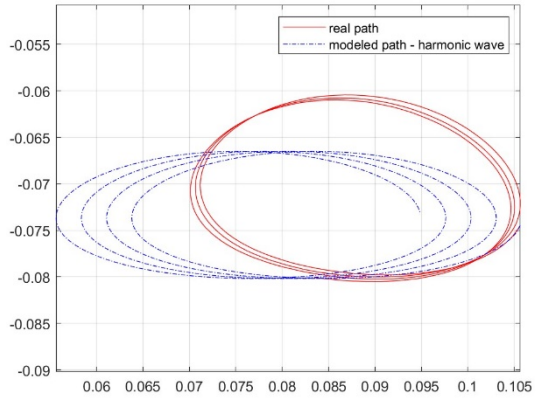

Figure 42: Trajectory 17, Fluid particle-linear theory.

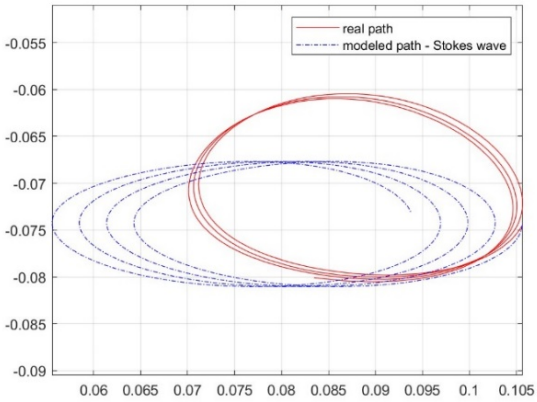

Figure 43: Trajectory 17, Fluid particle-Stokes theory.

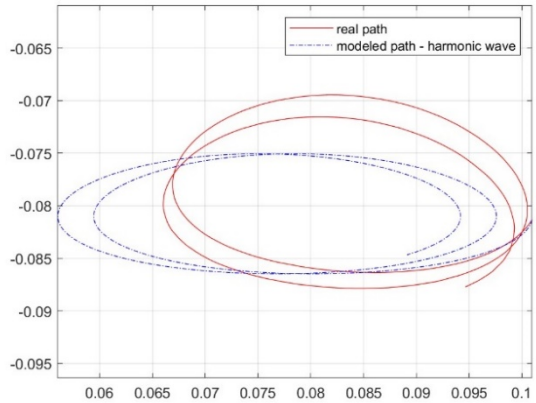

Figure 44: Trajectory 27, Fluid particle-linear theory.

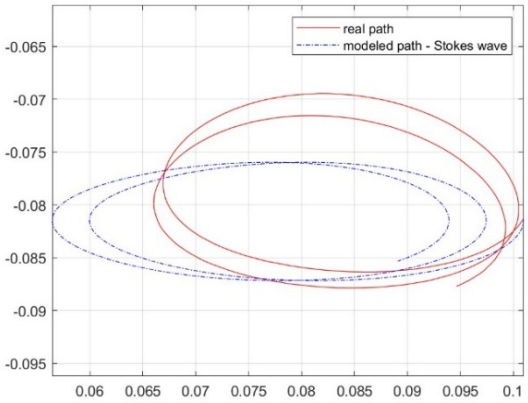

Figure 45: Trajectory 17, Fluid particle-Stokes theory.

In the script for inertial particles, both graphs associated with linear theory (Figs. 46, 48..) and graphs referring to Stokes theory (Figs. 47, 49..) have been generated.

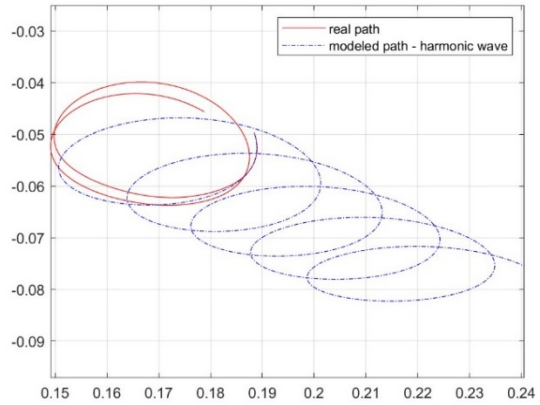

Figure 46: Trajectory 32, Inertial particle-linear theory.

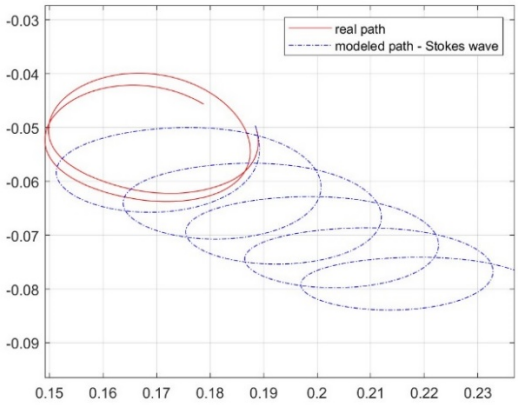

Figure 47: Trajectory 32, Inertial particle-Stokes theory.

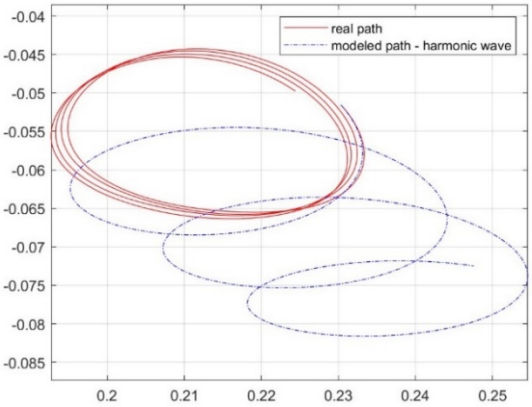

Figure 48: Trajectory 10, Inertial particle-linear theory.

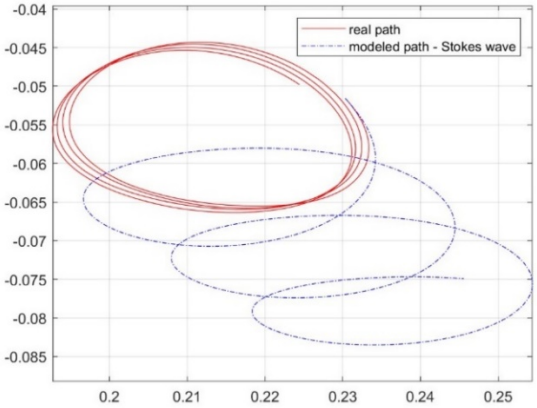

Figure 49: Trajectory 10, Inertial particle-Stokes theory.

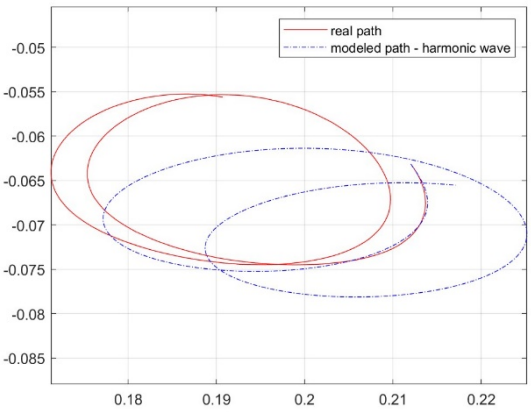

Figure 50: Trajectory 36, Inertial particle-linear theory.

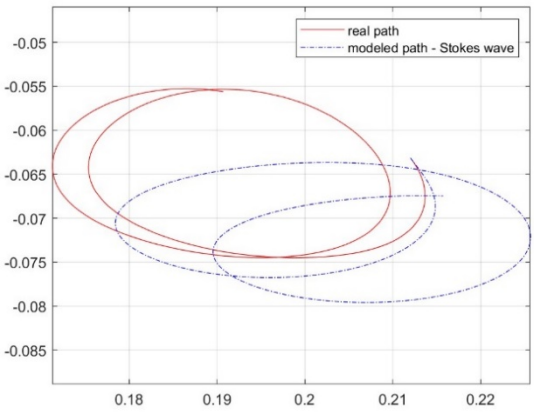

Figure 51: Trajectory 36 Inertial particle-Stokes theory.

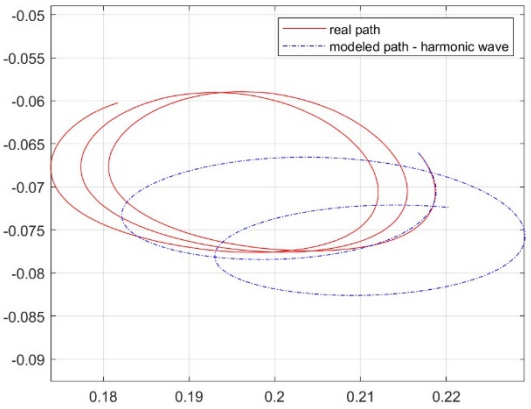

Figure 52: Trajectory 23, Inertial particle-linear theory.

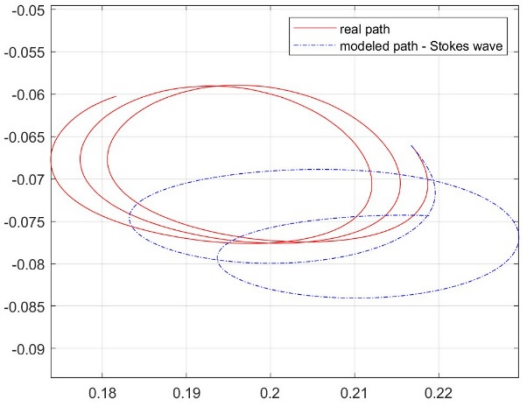

Figure 53: Trajectory 23, Inertial particle-Stokes theory.

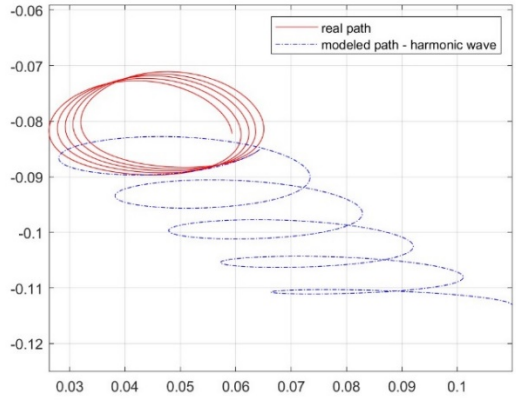

Figure 54: Trajectory 7, Inertial particle-linear theory.

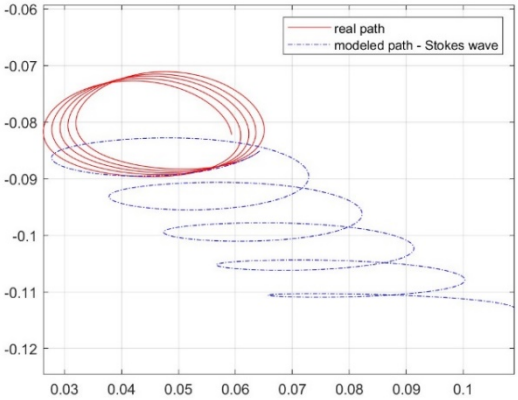

Figure 55: Trajectory 7, Inertial particle-Stokes theory.

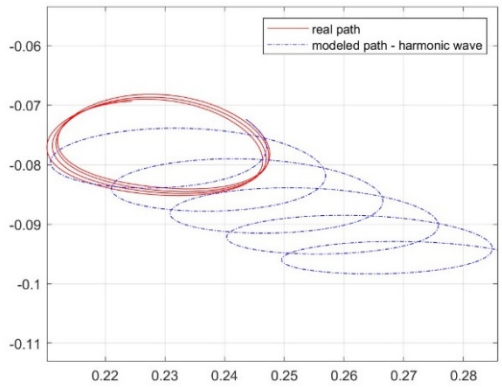

Figure 56: Trajectory 11, Inertial particle-linear theory.

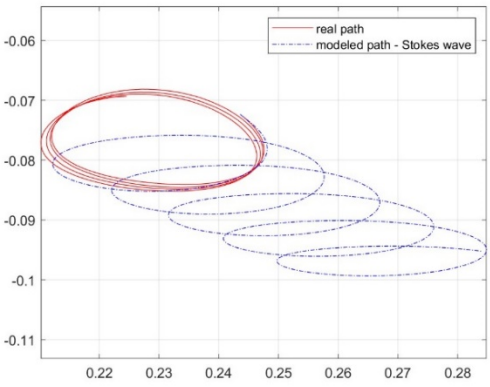

Figure 57: Trajectory 11, Inertial particle-Stokes theory.

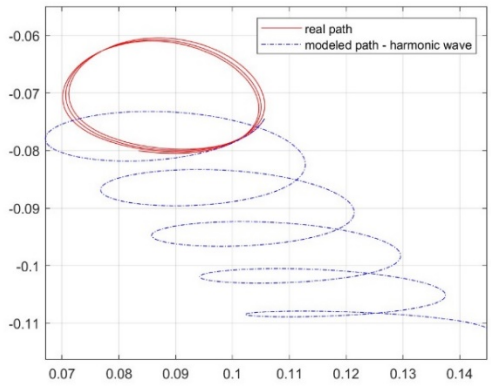

Figure 58: Trajectory 17, Inertial particle-linear theory.

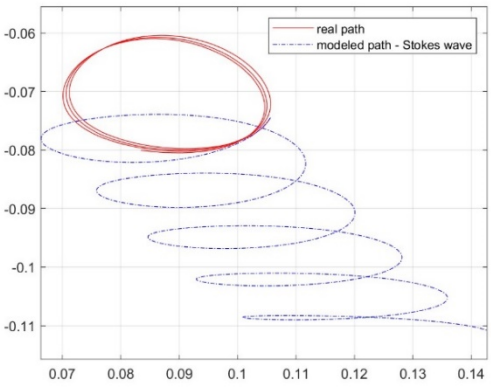

Figure 59: Trajectory 17, Inertial particle-Stokes theory.

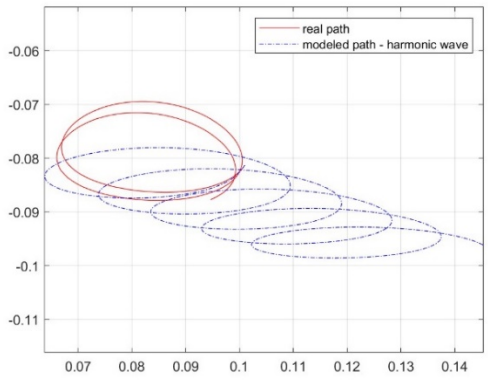

Figure 60: Trajectory 27, Inertial particle-linear theory.

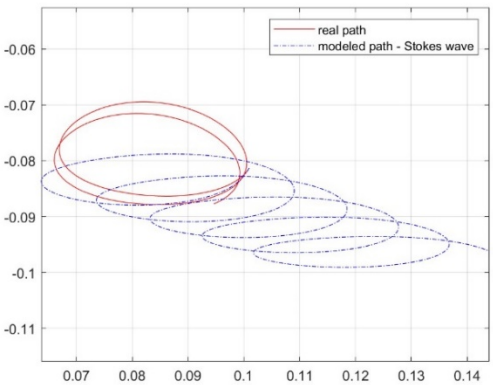

Figure 61: Trajectory 27, Inertial particle-Stokes theory.

When comparing the graphs obtained for each particle, it emerged that none of them exhibits behavior that can be attributed to an inertial particle. All the selected particles, however, show a behavior closer to that of a fluid particle. Consequently, we assumed as inappropriate to classify the four trajectories located close to the free surface as outliers. On the contrary, these trajectories must be considered when plotting the drift velocity adaptation curve.

The reason why the four trajectories were closer to the free surface than the rest of the group, however, is still unknown. To try to clarify this point, the drift velocity was recalculated in relation to depth, following the same methodology previously mentioned, focusing exclusively on the first loop of each trajectory.

Figure 62 presents the Drift trend, considering both the one calculated at the first loop of each particle (represented by the red dots) and the general one which takes into account the entire trajectory (represented by the blue dots). It is clear that there is no significant difference between the two approaches; the positions of the particles are essentially similar, except for particle 18.

Consequently, we could proceed with the polynomial fitting curve by including all particles, those obtained considering all the loops for each trajectory (blue dots), without excluding any as can be seen in Figure 63.

We believe that the placement of such particles can be attributed to a number of factors, including how the seeding was released, along with the non-uniform shape and weight of each particle.

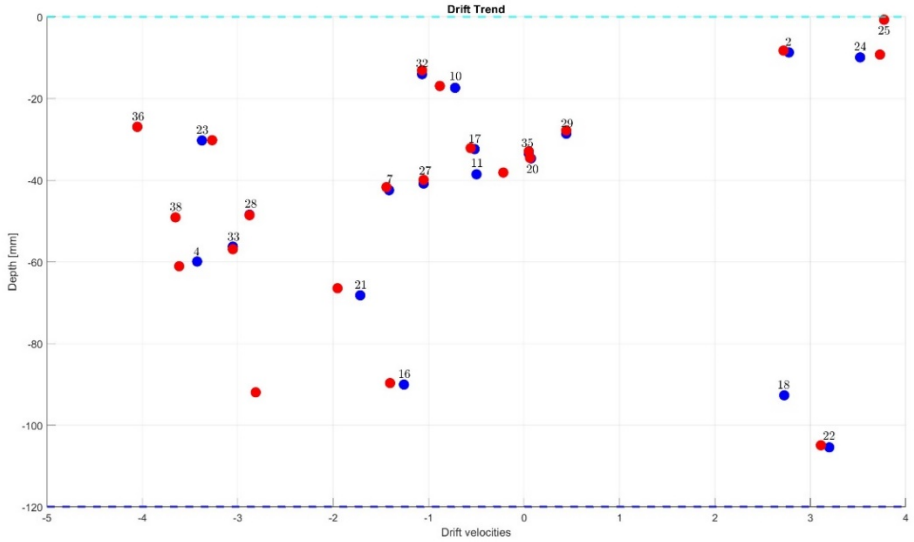

Figure 62: Drift trend.

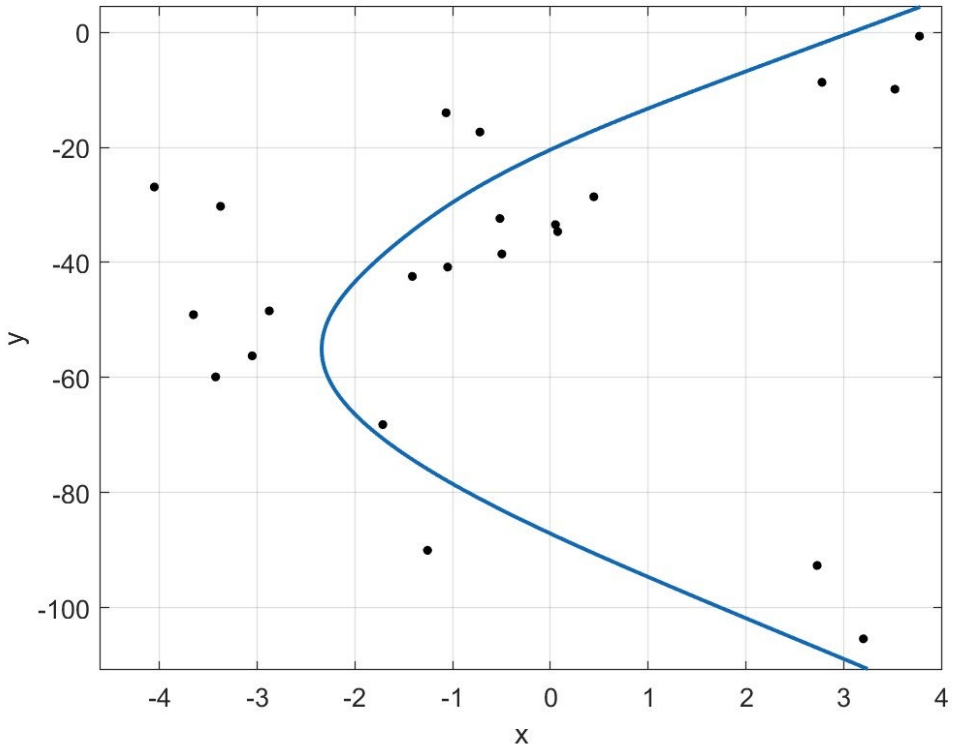

Figure 63: Fitting curve of drift trend.

3.4 Analysis of Bichromatic waves

The bichromatic waves were generated by superimposing a shorter wave onto a longer wave. The shorter component was based on the same characteristics of the above-mentioned monochromatic wave (*a1, T1*), while the longer component was characterized by a smaller amplitude and a longer period (*a2, T2*), with the aim to reproduce the natural combination of shorter sea waves with longer infragravity (IG hereafter) waves that typically occur in the nearshore region [2].

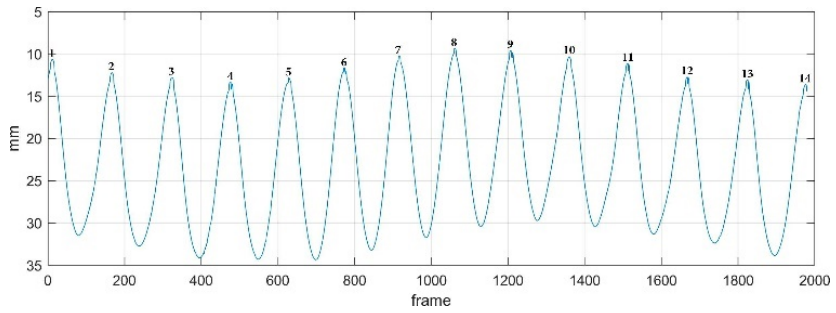

Figure 64: Free surface.

The figure 64 illustrates the free surface in millimetres calculated on two thousand frames. The vertical tracking line is located in the centre of the frame to avoid possible inaccuracies at the edges. It is evident that the height of the short wave varies within a long wave cycle. Therefore, we chose to analyze the frames relating to the fourth peak (corresponding to the IG trough) and the ninth peak (corresponding to the IG peak), both with a height of approximately 2 cm. It is clear that all waves are influenced by the non-linear interactions between the two superimposed waves, causing a vertical elongation, as in the case of wave 8.

The infragravity waves were analyzed following the same procedure used for the monochromatic waves.

After removal of the background, a reduced amount of seeding emerged compared to that used for the monochromatic wave throughout the entire water column, as highlighted in Figures 65 and 66.

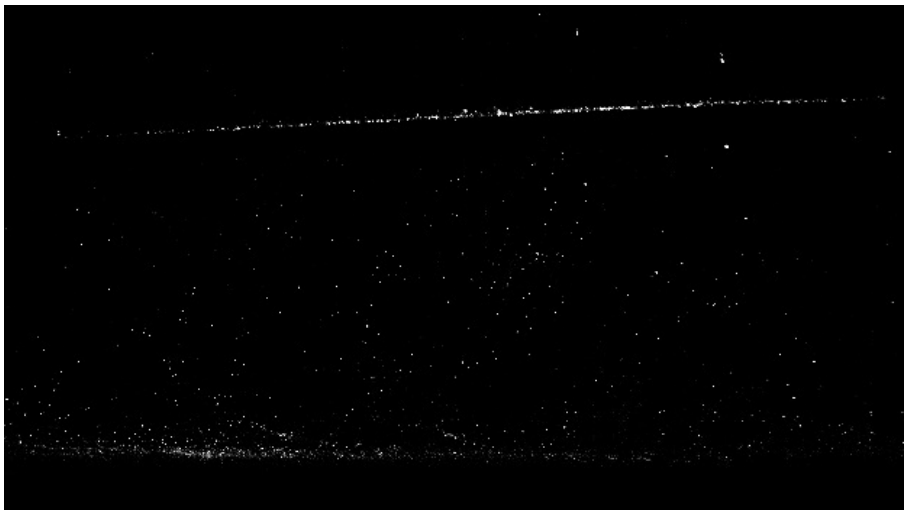

Figure 65: Shortwave particles on the trough.

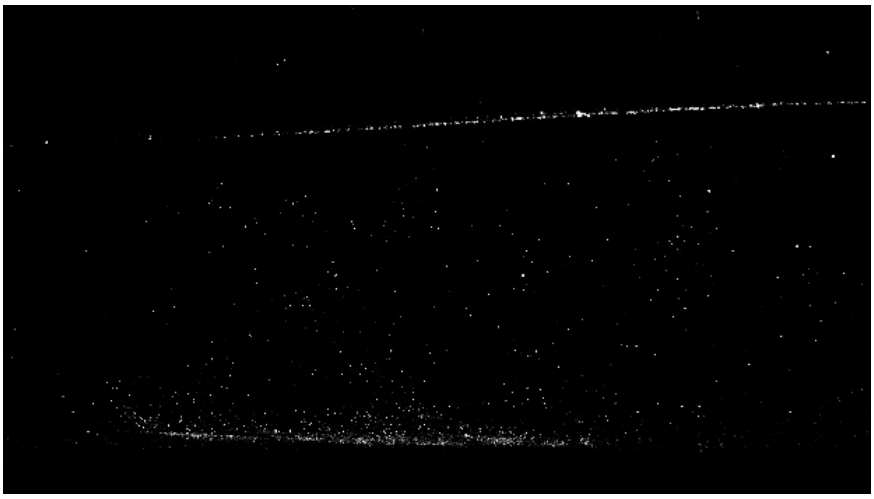

Figure 66: Shortwave particles on the peak.

The script VelocityFieldPhaseMean.m is designed to extract velocity profiles within a specific vertical column in the field of view. However, in this particular instance, the term phase mean is not applicable since only one phase is involved. Observing the values taken by "u" along the x-axis, it can be seen that the velocity profile oscillated between a maximum of 0.07 m/s and a minimum of -0.1 m/s for the short wave at the Ig trough (Figure 67), with the negative value indicating particle movement in the opposite direction to the wave propagation and between a maximum of 0.11 m/s and a minimum of -0.05 m/s for the short wave at the Ig peak (Figure 68).

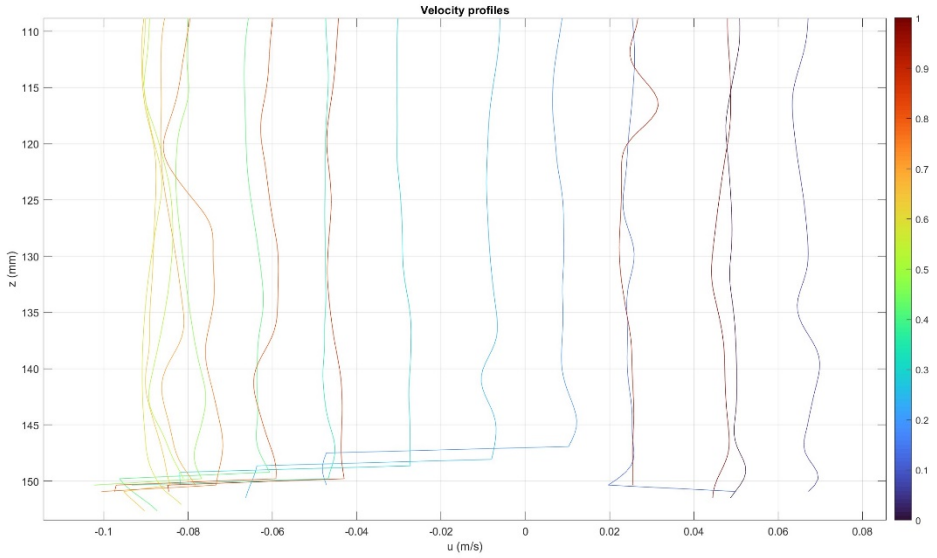

Figure 67: Selected velocity profiles at the IG trough.

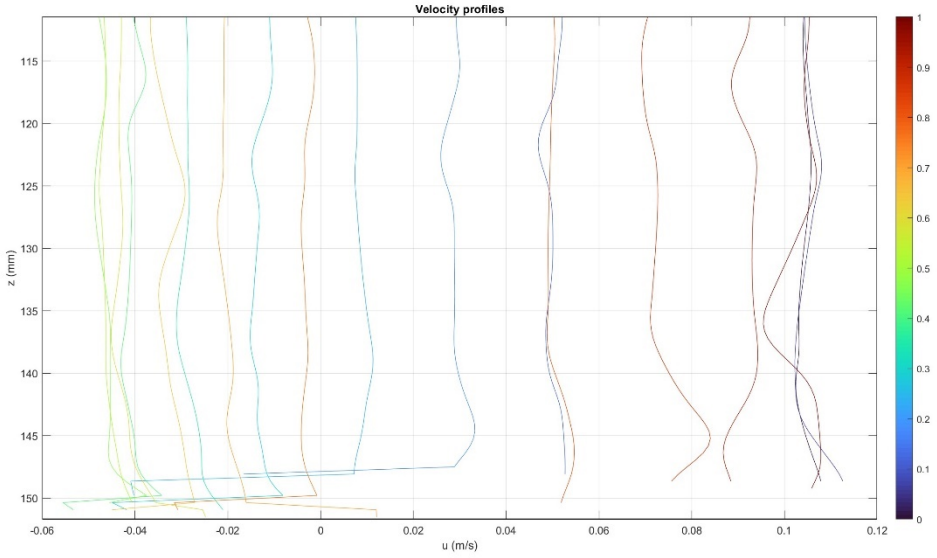

Figure 68: Selected velocity profiles at the IG peak.

Through the LongestTrajectories.m script, the trajectories were also traced for the bichromatic waves. As is evident in both figures (Fig. 69 and 70), the observed behaviour corresponds exactly to our expectations. In Figure 69, we refer to the short wave at the IG trough, where all trajectories appear to move in the opposite direction to the direction of wave propagation. This phenomenon occurs because near the trough of the infragravity wave, the wave propagates in the opposite direction, providing the trajectories with the corresponding horizontal drift, while

each loop is generated by the monochromatic wave that overlaps with the infragravity one. Similarly, we observe the same behaviour for the short wave at the IG peak (figure 70), where all trajectories show a net movement towards the right of the frame considering that the wave move from the left to the right. This happens because the short wave is propagating at the peak of the infragravity wave.

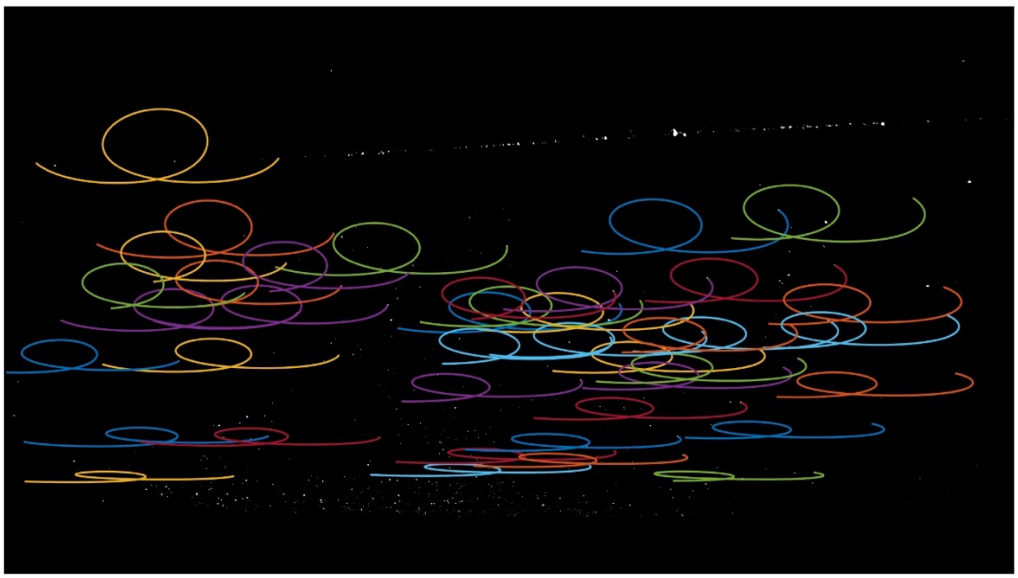

Figure 69: Short wave trajectories on the IG trough.

Figure 70: Short wave trajectories on the IG.

Next, the specific trajectories occurring on the wave 4 trough and wave 9 peak were examined in detail, see figure 64.

With regard to the trajectories associated with wave trough 4, only those that recorded their positions between frames 45 and 200 of the pertaining frame package were taken into account, as illustrated in figure 71. This interval was selected as those frames delimited the short wave placed in the IG trough: i.e. wave 4 in Figure 64.

With regard to the trajectories linked to the peak of wave 9, showing a clear position in frames 40 and 186 of the pertaining frame package were analysed (Figure 72).

This interval was chosen as those frames delimited the short wave placed in the IG peak: i.e. wave 9 in Figure 64.

In both figures, the x-axis shows the number of frames, from which it is easy to obtain the Lagrangian period, while on the y-axis we have the calculated position relative to the x-axis, from which we can derive the horizontal drift.

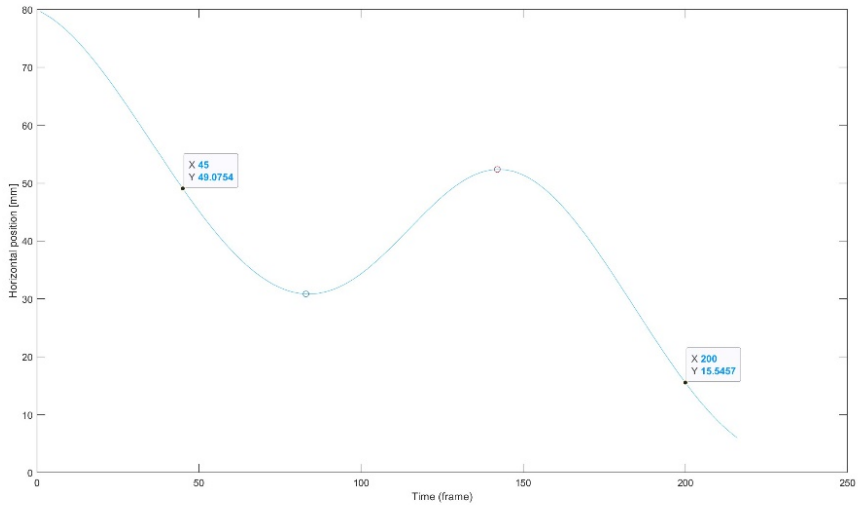

Figure 71: Graphic on the x-axis relative to the Short wave trajectories at the IG trough.

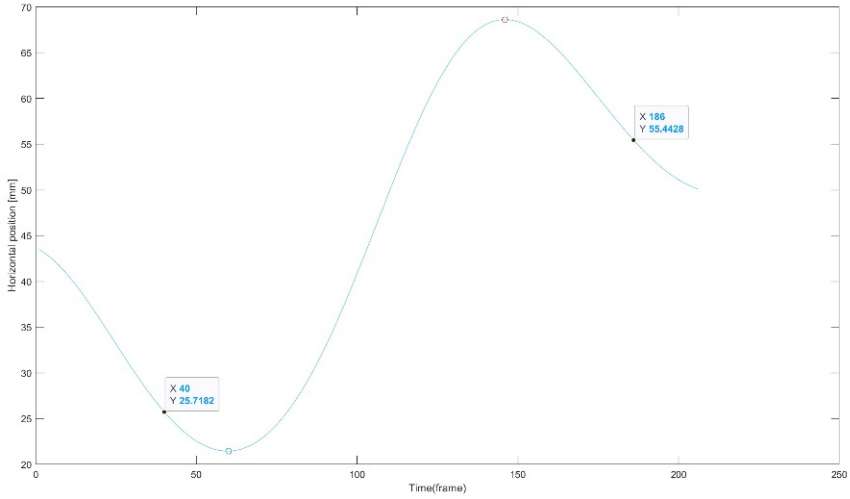

Figure 72: Graphic on the x-axis relative to the Short wave trajectories at the IG peak.

For both configurations, a graph was created displaying the drift velocities in relation to depth (see Figures 73 and 74). As is evident from the graphs in Figures 69 and 70, these representations were processed during the first cycle of each trajectory.

Both the drift velocity and the depth of each trajectory were calculated using the same approach as for the monochromatic waves.

The drift velocities were determined by calculating the difference in the horizontal drift and dividing it by the Lagrangian period, see Figures 71 and 72.

As for the position of each particle within the wave (depth), the midpoint between a maximum and minimum of the graph obtained on the y-values was calculated, following the same methodology used for the monochromatic waves.

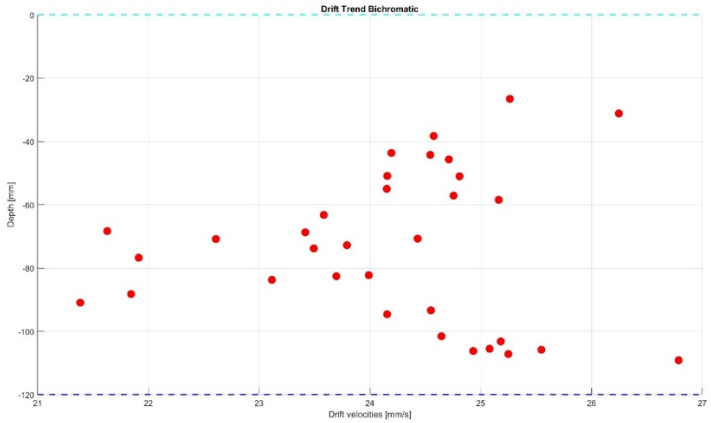

Figure 73: Drift trend about the short-wave trajectories on the IG peak.

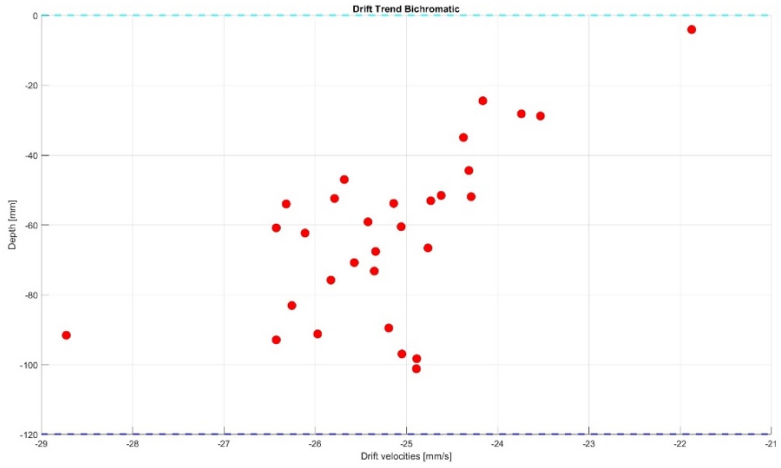

Figure 74: Drift trend about the short-wave trajectories on the IG trough.

For the trajectories associated with the short wave on the IG trough, an average drift velocity of -25.1938 mm/s is obtained, with a standard deviation of 1.1858. As for the trajectories associated with the short wave on the IG wave peak, the average velocity is 24.1700 mm/s, with a standard deviation of 1.2579.

Finally, for a better identification of the behaviour of the drift velocities, fitting curves were plotted using a second-degree polynomial equation, as illustrated in Figures 75 and 76.

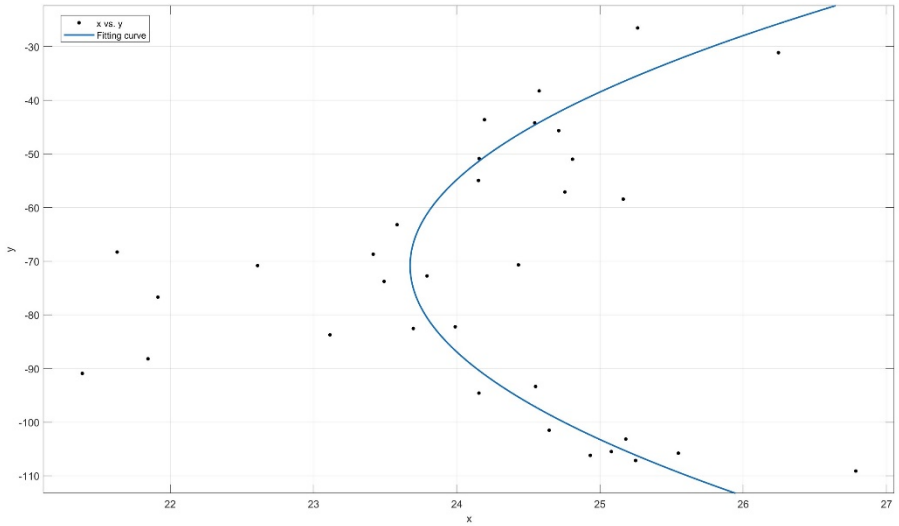

Figure 75: Fitting curve of short-wave trajectories on the IG peak.

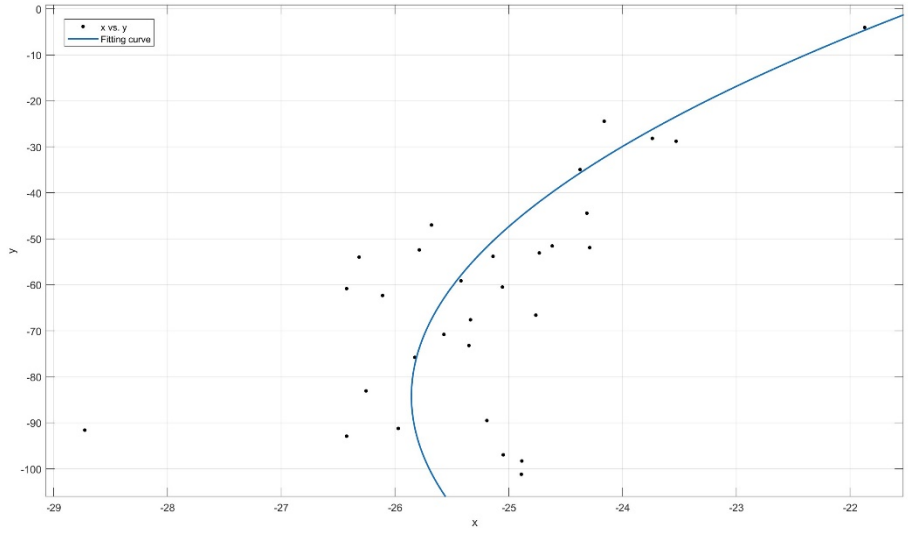

Figure 76: Fitting curve of short-wave trajectories on the IG trough.

4 Discussion

In this context, this thesis aims to analyze two types of waves: monochromatic and bichromatic, characterizing their differences and examining the related effects. Particular attention is paid to velocity fields, the tracking of particle trajectories within the waves and the trend of drift velocity.

As regards the monochromatic wave, a velocity profile was obtained that oscillates between a maximum of 0.1 m/s and a minimum of -0.1 m/s, presenting a symmetrical trend (see figure 17).

As highlighted in figure 67, for the bichromatic wave, however, the velocity profile oscillates between a minimum of -0.1 m/s and a maximum of 0.06 m/s for the short wave on the IG trough and between -0.06 and 0.1 for the short wave on the IG peak (figure 68). This phenomenon is attributable to the influence of the short wave on the long wave, determining a greater negative velocity in the first case and a greater positive velocity in the second.

The validity of these results is further highlighted in graphs 69 and 70 where the trajectories of the particles in the short wave on the IG trough show a negative drift, i.e. opposite to the propagation of the wave, while the trajectories in the short wave on the IG peak show a positive behavior.

The average drift velocity of the monochromatic wave was calculated, which stands at 2.0566 mm/s, representing approximately 8.31% of the average drift velocity (24.6819 mm/s) calculated between the short wave on the trough and that on the peak of the IG wave.

Similarly, the standard deviation of the monochromatic wave, equal to 2.4482, is approximately double the average of the standard deviation of the two bichromatic configurations, which amounts to 1.22185.

The graph relating to the drift trend of the monochromatic wave, described in the results chapter, has been dimensionally normalized in order to facilitate comparison with the experiments conducted by Grue and Kolaas [6].

Comparisons with calculations from the inviscid and strongly nonlinear Fenton method and second-order theory show that flow velocities in the boundary layers below the wave surface and above the fluid bottom contribute to a forward drift

velocity and to an excess period strongly increased. Furthermore, they showed that the experimental cutoff of the drift velocity becomes more than double that obtained with the Fenton method, which in turn is about double that of the second-order theory near the surface.

Observing the trend of the blue line in figures 77 and 78, qualitative similarity between our results and the Grue and Kolaas's results is evident (figure 77).

Both drift velocities appear to exhibit similar behavior, below the wave surface and above the bottom, they contribute to a notable increase in the forward drift velocity. On the contrary, they become clearly negative in the center of the water column.

This would confirm that the measured Lagrangian drift velocity, systematically in excess of inviscid theories, indicates that wave-induced Stokes drift is significantly higher than that commonly represented in wave-current interaction models.

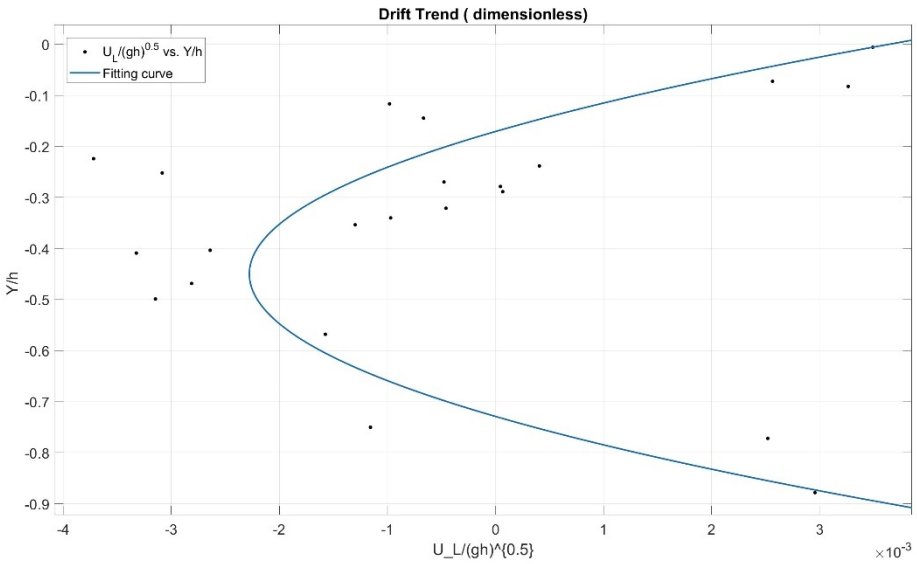

Figure 77: Drift trend of monochromatic wave (dimensionless).

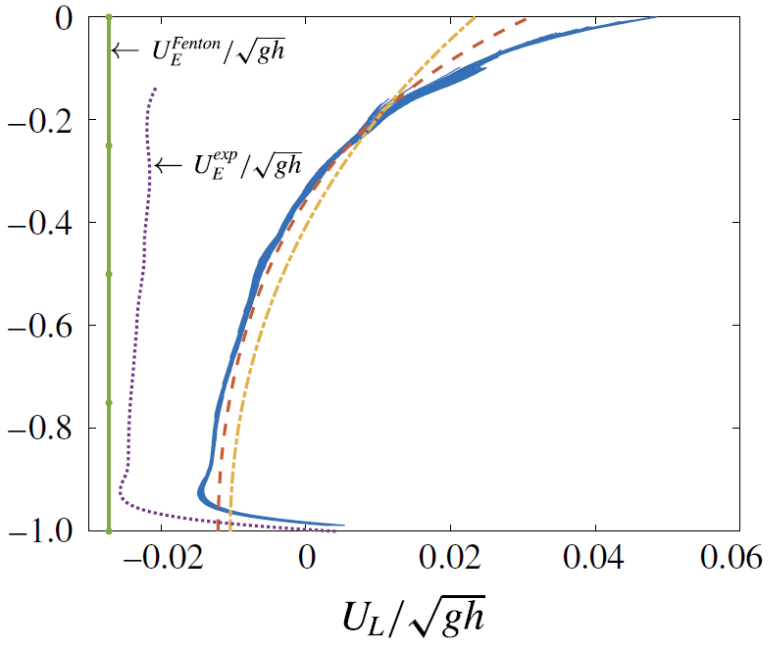

Figure 78: Horizontal drift velocity UL for time window 1 (t~9:9–13:8 s). (J. Grue and J. Kolaas 2017).

If we focus our attention only on the drift velocities of the bichromatic wave, we notice that they are almost similar. In particular, the drift velocity of the short wave at the trough (-25.1938 mm/s) is of approximately 97.54%, lower than the celerity wave, i.e. 1.08 m/s, while that of the short wave at the peak (24.1700 mm/s) is approximately 97.7% lower.

Analyzing figures 73 and 74, two distinct behaviors emerge in terms of drift velocity.

In the graph relating to the peak of the IG wave, a greater drift velocity is highlighted at the walls (i.e water surface and seabed), suggesting a greater particle concetration in the central area.

On the contrary, in the short wave at the IG trough, the absolute drift velocity is greater in the central area, indicating a greater presence of particles at the walls.

These results may be of considerable interest in the context of tracers, pollutants or marine debris. Through such data, it is possible to understand the behavior of such elements both on the trough and on the peak of real-world IG wave.

5 Conclusion

An experimental setup provided at the Laboratory of Hydraulics and Maritime Construction of the Polytechnic University of Marche (Ancona) was used to carry out experimental tests on monochromatic and bichromatic waves, to study the drift velocity along the water column. In the channel, two series of experiments were conducted, characterized by a height of 3 cm and a period of 1 s for the monochromatic test and a combination of a short wave (height of 3 cm and 1 period of 1s) and a long wave (height of 0.3 cm and a period of 10s).

The tracer used was chili pepper, chosen for being neutral with respect to the water present in the channel.

The experience acquired has provided various insights, both from a theoretical and practical point of view, especially in relation to the various configurations to be studied.

Software like Matlab and toolboxes like Part2Track have made it possible to complete what was done in the laboratory. Their functionalities were used for post-processing, which provided the results which are the object of study of this thesis.

These results take on a role of particular relevance in the context of environmental management and marine safety, especially in relation to tracers, pollutants or marine debris. Detailed analysis of trajectories and drift velocities provides an in-depth perspective on the behavior of such elements along the trough and peak of the bichromatic wave.
By collecting accurate data, we are able to gain a clearer understanding of how these elements interact with the marine environment. This allows one to outline dispersal paths, identify any significant concentrations, and evaluate the possible impact of these elements on marine ecosystems.

Furthermore, the ability to model the motion of tracers or debris in different oceanographic conditions can be fundamental for the development of environmental management and emergency response strategies.

Using such data ultimately helps inform crucial decisions regarding ocean protection and environmental sustainability.

To delve deeper and clarify this topic in the best possible way, further analysis would be needed, considering that the entire study covered by the thesis is preliminary.

In optimal test conditions, the experiment could be repeated, for example considering longer wave cycles, in order to have more sections at the trough and at the peak, average them and then make a comparison.

Future developments would be desirable, both in terms of more detailed research and new experiments.

References

[1] Baldock, T. E., Huntley, D. A., Bird, P. a. D., O'Hare, T. J., & Bullock, G. N. (2000). Breakpoint generated surf beat induced by bichromatic wave groups. *Coastal Engineering*, *39*(2–4), 213–242. https://doi.org/10.1016/s0378-3839(99)00061-7.

[2] Bertin, X., De Bakker, A., Van Dongeren, A., Coco, G., André, G., Ardhuin, F., Bonneton, P., Bouchette, F., Castelle, B., Crawford, W., Davidson, M., Deen, M., Dodet, G., Guérin, T., Inch, K., Leckler, F., McCall, R., Müller, H., Olabarrieta, M., . . . Tissier, M. (2018). Infragravity waves: From driving mechanisms to impacts. *Earth-Science Reviews*, *177*, 774–799. https://doi.org/10.1016/j.earscirev.2018.01.002.

[3] Bjørnestad, M., Buckley, M., Kalisch, H., Streßer, M., Horstmann, J., Frøysa, H. G., Ige, O. E., Cysewski, M., & Carrasco-Alvarez, R. (2021). Lagrangian measurements of orbital velocities in the surf zone. *Geophysical Research Letters*, *48*(21). https://doi.org/10.1029/2021gl095722.

[4] De Bakker, A.T.M., Tissier, M.F.S., Ruessink, B.G., 2015b. Beach steepness effects on nonlinear infragravity-wave interactions: a numerical study. J. Geophys. Res. 121. http://dx.doi.org/10.1002/2015JC011268.

[5] Itay, U., & Liberzon, D. (2017). Lagrangian kinematic criterion for the breaking of shoaling waves. *Journal of Physical Oceanography*, *47*(4), 827–833. https://doi.org/10.1175/jpo-d-16-0289.1.

[6] J. Grue and J. Kolaas. Experimental particle paths and drift velocity in steep waves at finite water depth. Journal of Fluid Mechanics, 810(R1):1{10, 2017.

[7] Janke, T., Schwarze, R., & Bauer, K. (2020). Part2Track: A MATLAB package for double frame and time resolved Particle Tracking Velocimetry. *SoftwareX*, *11*, 100413. https://doi.org/10.1016/j.softx.2020.100413.

[8] Longuet-Higgins, M., Stewart, R., 1962. Radiation stress and mass transport in gravity waves, with application to surf beats. J. Fluid Mech. 13, 481–504. http://dx.doi.org/ 10.1017/S0022112062000877.

[9] Monismith, S. G., Cowen, E. A., Nepf, H. M., Magnaudet, J., & Thais, L. (2007). Laboratory observations of mean flows under surface gravity waves. *Journal of Fluid Mechanics*, *573*, 131-147.

[10] M. Tucker. Surf beats: Sea waves of 1 to 5 min. period. Proceedings of the Royal Society of London. Series A. Mathematical and Physical Sciences,202(1071):565{573, 1950.

[11] P. K. Kundu, I. M. Cohen, and D. Dowling. Fluid mechanics 6th, 2016.

[12] Santamaria, F., Boffetta, G., Afonso, M. M., Mazzino, A., Onorato, M., & Pugliese, D. (2013). Stokes drift for inertial particles transported by water waves. A Letters Journal Exploring, 102(1), 14003. https://doi.org/10.1209/0295-5075/102/14003.

[13] T. Van Den Bremer and _. Breivik. Stokes drift. Philosophical Transactions of the Royal Society A: Mathematical, Physical and Engineering Sciences,376(2111):20170104, 2018.

[14] W. Munk. Surf beats. EOS, Transactions American Geophysical Union,30(6):849{854, 1949.

[15] Webb, S.C., 2007. The earth's ‘hum’ is driven by ocean waves over the continental shelves. Nature 445, 754–756. http://dx.doi.org/10.1038/nature05536.

Acknowledgments

First of all, I would like to thank my supervisor, Matteo Postacchini. I am grateful that you introduced me to the study of waves and gave me the opportunity to participate in your field experiments. Your constant help and professionalism have allowed me to work day after day in a clear and concrete way. Thanks to your empathetic attitude in relating to students, I was able to undertake this journey without ever feeling the typical distance between a professor and a student. Your relationality made every moment of this experience meaningful and full of value.

To my co-supervisor Lorenzo Melito, thank you for always taking the time to help me. I never felt alone for a moment, I always knew I could count on you. You have been a great support and have made studying this topic even more fun.

I would also like to dedicate some words to Prof. Henrik Kalish to express my deep gratitude for all the support, guidance, and incredible opportunity you provided me during my internship in Norway. These two months have been an extraordinary and formative experience. Your attentive and patient guidance made my learning journey much smoother. Moreover, the fact that you made my stay in Bergen possible was a dream come true. I was fortunate to explore a new culture, meet extraordinary people, and significantly broaden my horizons. This experience will be a treasure that I will always carry with me.

I would also like to thank the administration at the department for being so friendly and helping me out with whatever needed!

Lastly, I would like to thanks to my family for always cheering on me. Staying motivated throughout this year was a lot easier because of you and your support means a lot to me! And thanks for the lifelong friends who know more than anyone how complicated it was for me to finish this journey.
You have always been close to me, especially in the most complicated moments and have allowed me to never give up.